Velocity measurements in a fiber suspension flow: formation of a fiber network

by

Gabriele Bellani

October 2008
Technical Reports from
Royal Institute of Technology
KTH Mechanics
SE-100 44 Stockholm, Sweden

Akademisk avhandling som med tillstånd av Kungliga Tekniska Högskolan i Stockholm framlägges till offentlig granskning för avläggande av teknologie licentiatsexamen den 29 oktober 2008 kl 10.15 i Sundbladsalen, Drottning Kristinas Väg 61, STFI-Packforsk, Stockholm.

Universitetsservice US–AB, Stockholm 2008

Gabriele Bellani 2008, **Velocity measurements in a fiber suspension flow: formation of a fiber network**

Linné FLOW Centre
KTH Mechanics
SE–100 44 Stockholm, Sweden

Abstract

The aim of the present work is to experimentally study the dynamics of the formation of a fiber network formed from the filtration of a fiber suspension. This is relevant for all industrial applications (*e.g.* papermaking, productions of composite material, *etc.*) where a suspension of fibers has to flow through narrow gaps, and the quality of the product depends on the distribution of mass and orientation of the fibers.

To study the dynamics of network formation, we developed an experimental setup where the filtration of a fiber suspension through a semi-permeable screen can be studied. In the setup, both the fluid and the solid phase can be visualized.

The focus of the present thesis is to study the fluid flow generated during the filtration.

Index of refraction matching, image processing and particle image velocimetry have been used to measure the velocity field in the proximity of the resulting fiber network. Experiments with varying fiber length and filtration velocity have been performed.

The disturbances generated by the screen and the forming network was found to be confined in a region (*boundary region*), whose extension varies with time: first, after the formation of the first fiber layers, the extent of the boundary region increases; at later times, the boundary region is thinner. The extent appears to be correlated to the gap size either of the screen (at very early times) or of the fiber network, but independent of the filtration velocity.

Fluctuations on a scale larger than a fiber length are also observed during the filtration process. These fluctuations are found to be correlated to the non-dimensional number Se that relates the sedimentation velocity of a fiber to the filtration velocity.

The governing non-dimensional parameters are derived from the equations. The parameters are used to relate the experimental observations to the dewatering process in papermaking.

Descriptors: Fluid mechanics, Fiber suspension, Fiber network, PIV, Index of Refraction, Digital image processing.

Parts of this work have been presented at:

Svenska mekanikdagarna,
13 – 15 June 2007, *Luleå, Sweden*

6th International Conference on Multiphase Flow, ICMF 2007[1],
9 – 13 July 2007, *Leipzig, Germany*

The Fourth International Conference on Flow Dynamics, ICFD2007[2],
26 – 28 September 2007, *Sendai, Japan*

TAPPI/PIMA PaperCon 08[3],
3 – 7 May 2008, *Dallas, Texas, USA*

[1] With written contribution to the conference proceedings: G. Bellani, F. Lundell and L. D. Söderberg, "A study on formation of fibre networks with PIV at high particle concentrations".

[2] The presentation received the *"Best presentation award for student"*.

[3] With written contribution to the conference proceedings: G. Bellani, F. Lundell and L. D. Söderberg, "Experimental study of the forming process: fluid velocity and fluid-fiber interaction measurements".

Per nonno Alberto

Contents

CHAPTER 1

Introduction

This work is an experimental study on the formation of a fiber network through filtration of an initially dilute fiber suspension. This process is dominated by complicated interactions between the solid (fibers) and the liquid phase. Our aim is to develop experimental tools that allow real time observations, and measurements on the flow generated during the filtration, to capture the fundamental aspects of the dynamics of the formation of the network. The formation of a network from a diluted suspension is the core of papermaking, and a deeper understanding of the fundamental physics can provide new tools for improving the whole process of paper manufacturing. This introduction therefore starts with an overview of papermaking followed by introductions to fiber-suspension flows and multiphase-flow measurements.

1.1. Papermaking: the art and the science

The process of papermaking involves a mixture of fibers and water (*i.e.* a *fiber suspension*). In order to make paper, the fibers have to be efficiently dispersed, oriented and de-hydrated. These operations involve interactions of fibers with time-dependent, turbulent flows in complicated geometries (channels, contractions, pipes, permeable wires, *etc.*), and at present, complete theoretical descriptions of such flows are not available.

For these reasons, the modern process of paper forming represent a big challenge for the engineers, and a gold mine of unanswered questions for the researchers.

The primary sources of information for this chapter are Söderberg (1999), Holm (2005), Deng & Dodson (1994) and Petrie (1999).

1.1.1. *History*

Cellulose fibers possess an almost magic property: when they are dissolved in water they do not stick together, but as soon as the water is removed, chemical bonds start to form naturally, creating a strong network. If you do this operation properly, this network becomes what is universally known as *paper*.

The first to discover this secret were the Chinese, almost two thousand years ago. To testify this, there is a paper manuscript conserved in the British Museum containing chinese characters, dated at A.D. 105.

Craftsmen in Central Asia remained the only ones able to manufacture paper sheets until the eight century, when, according to the legend (Quraishi 1989), the secret of papermaking was obtained from two chinese prisoners in the arab city of Samarkand. Thanks to the information they had grasped, the Arabs were able not only to start their own production in Baghdad, but they also developed a method to produce a thicker and more robust paper.

We can imagine that paper appeared for the first time in Europe at Christmas A. D. 800, when the Khalif of Baghdad sent a message on the precious material, to greet Charle-Magne, the new emperor of the Holy Roman Empire.

However, it took almost another four hundred years until the first paper mill was built in Europe, at Xátiva (modern Valencia) in 1120. After the first one, additional mills appeared in Fabriano, Italy, in the 13th century, as an import from Islamic Spain.

Production of paper became well established in Germany and Italy, and from there it spread to the rest of Europe.

Thanks to the extraordinary properties of its structure, paper became the preferred support for woodcut printmaking first and for movable type later, and since then, paper has given a great contribution to the transmission and to the advancement of the human knowledge.

Today, in the era of electronics, paper might not be the preferred mean of transmission of culture and information anymore, but it certainly maintains its central role in another industry. The industry of packaging.

That is, in a global world, paper might be less crucial for the exchange of ideas, but it is indispensable for the circulation of goods!

1.1.2. *From hand-sheets to paper machines*

Strength and characteristics of paper are determined during the process of forming, which contains the following steps:

(i) Dissolve cellulose fibers in a liquid (water), until the suspension reach the desired concentration.
(ii) Put the suspension on top of a permeable surface (wire) and stir to achieve a homogeneous distribution of fibers.
(iii) Allow water to flow through the wire, while the fibers are retained.
(vi) Remove the residual water by pressing the fibers between two blankets.
(v) Let the rest of the water evaporate until the sheet is dry.

Until the 18th century, paper sheets were manufactured one at a time by hand and their quality was dependent on the skill of the individual craftsman.

However this was a tedious and time consuming process. At the end of the 18th century, Nicholas Louis Robert of Essonnes introduced a machine which could produce paper in a continuous process. This first type of machine is now know as Fourdrinier former[1].

Machines do not posses the same adaptivity as the human brain and many improvements had to be done in order to achieve a quality level comparable to that of hand-made sheets. For many years, machine designers and papermakers worked on the base of trial and error, because of the lack of knowledge of the underlying physics. However in the last decades, the possibilities offered by modern computers and new measurement techniques, allow the problems to be tackled with a more scientific approach. As a results of this constant effort, papermakers have obtained considerable improvements: at present, paper comes out of the mill at a rate of more than 300 m^2/s, and its density is uniform on a scale on the order of the millimeter, or less! Although these are remarkable achievements, the increasing demand in production speed, environmental restrictions on usage of precious material like forest products and tight specifications of sophisticated commercial printing operations constantly require further improvements. To reach these goals, it is necessary to expand our understanding of all the phenomena that appear in the process of papermaking.

1.1.3. *The paper machine*

The advent of paper machines did not change the basic principles needed to transform a source of wood pulp into a final paper product, therefore a paper machine must be able to accomplish the steps described in the previous section.

The process of creating the fiber suspension (step (i)) is called *stock preparation*. Strictly speaking, a paper machine does not accomplish this step, since the stock preparation takes place somewhere else. What comes out from this process is a suspension of typically 3% concentration of cellulose fibers in water[2]. In addition to the fibers, the suspension contains also chemical additives that facilitate the creation of bonds, residuals of fibers (*fines*) and particles (like clay, SiO_2, etc.) added to reduce the need of expensive material coming from the wood or to improve the optical qualities of the paper (referred to as *fillers*). In the stock preparation the aim is also to select and modify the characteristic of the fibers according to the specific need of the mill.

According to step (ii) on paragraph 1.1.2, the suspension has to be homogeneously distributed over a permeable wire. The part of the paper machine that has to accomplish this task is called *headbox*. The headbox is a nozzle that,

[1]Nicholas Louis Robert of Essonnes (France) was granted a patent for a continuous paper making machine in 1799. However the name comes from the Fourdrinier brothers, who, a few years later, would build an improved version of the machine in England.

[2]This thick stock is successively diluted and the suspension that enters the headbox has a concentration of 0.5%-1%.

when is fed by the fiber suspension, creates an up to 10 m wide jet of typically 10-15 mm of thickness. This jet will impinge one (or two) moving permeable wire(s) on which the paper begins to form. In the headbox, the suspension is made homogeneous in two ways: first the suspension, which enters the headbox from a tube bank, is stirred by the turbulence generated at the inlet, then it is strained in the contraction which accelerates the flow and transforms the channel flow into a plane jet. In particular, the strain induced by the contraction seems to act very efficiently on dissolving agglomerates (called *flocs*) that fibers tend to form (Kao & Mason 1975). This is extremely important because the flocs have in general a detrimental effect on the paper quality. The contraction is very effective also in damping the turbulence generated at the inlet, and a low turbulence level is vital for the stability of the jet. Jet instabilities show strong correlation with the structure of the paper, as Söderberg (1999) discussed extensively.

The initial removal of water (*dewatering*) (see (iii)) begins when the jet hits the permeable bands[3]. These bands allow the water to flow through the gaps, while retaining the fibers. They move at approximately the same speed as the jet, although a slight speed difference is usually set since this has been observed to have a positive effect on the paper quality.

In the earliest design, the jet landed on a single horizontal wire and the dewatering occurred thanks to gravity. Later on, suction boxes were introduced to enhance the dewatering capacity. However, increased operational speed induced an instability of the wire. The onset of the instability is the bottleneck for the maximum production rate of this configuration.

In the modern machines, engineers overcame this problem by enclosing the suspension between two wires[4], which additionally provide the potential of producing a more symmetric paper. In twin-wire forming the dewatering pressure is produced either by a roll (*roll-forming*) or blades (*blade-forming*) which impart a strong local deflection of the wire. The latter method produces localized pressure pulses that introduce the benefit of breaking up fiber flocs, but also the detrimental effect of reducing paper strength (The details of the origin of pressure pulses can be found in Holmqvist (2005)). A combination of roll and blade forming is the most common design in the present paper machines.

After the initial dewatering, more than 95% of the water has been removed and the solid content in the fiber network has become about 12-15%. To remove the last fraction of water, the wet web is sent to the pressing and drying sections, which complete steps (iv) and (v). The drying section is the largest part in

[3]Terminology for the permeable bands is not unique in literature, common denomination are *forming fabric* or *wires*.
[4]The process of making paper using two wires is known as *twin-wire forming*.

the paper machine since considerable amount of time (and energy) is needed to remove the last water.

Pressing and drying involve a huge amount of energy, thus their optimization is crucial (for more details, see Vomhoff (1998)). However, since the mobility of the fibers in the network at this stage is very limited, the hydrodynamic interactions cannot affect the fiber distribution anymore. For this reason, in the next section we shall concentrate on the forming section, and in particular on the initial dewatering.

1.1.4. *Initial dewatering*

Initial dewatering begins when the jet coming from the headbox hits the forming wire. In this phase, the dilute suspension coming from the headbox is filtered through the wires, and the fiber network begins to form. At the end of the dewatering, this network will have a concentration of about 12-15%. Knowing the jet speed (30 m/s), the jet thickness ($\approx$ 10 mm) and the forming length ($\approx$ 2-3 m), the average velocity of the dewatering flow can be estimated to be around 0.1 m/s. This information will be used later, to compare it with the experimental conditions in the present study.

As mentioned in the previous section, the final distribution of fibers in the network will be mainly determined in this phase, because after it, the mobility of the fibers will be very limited. The distribution of fibers in the network is directly related to an important property of paper: the *grammage* distribution. Grammage w is defined as weight per unit area (g/m^2), and paper quality is for many aspects determined by the local grammage variation. A measure of the grammage variation commonly used in the papermaking industry is the *Formation number* F:

$$F = \sigma(w)/w_m \tag{1.1}$$

where σ represent the operation of standard deviation and w_m is the average grammage. In other words, an high Formation number means high variation of the local grammage, thus a non-uniform distribution of fibers in the network. It has to be pointed out that the formation number as defined in equation 1.1 valuable information on the scales of grammage variation are lost. To overcome this problem, other methods based on spectral analysis are often applied.

Many studies report how the dewatering phase affects the Formation number. In particular Norman (1995), analyzing the formation spectra, observed that there is an inherent self-healing effect in the dewatering process, which can make a real sheet more evan than a random sheet[5]. This has been shown experimentally also by Lucisano & Norman (1994). The self healing has been discussed also in Sampson *et al.* (1995).

[5]A sheet with a random distribution of fibers. This was believed to be the upper limit in the homogeneity of a real sheet.

The general explanation given for the self-healing effect is that a region of the web with lower density at a certain time during the dewatering have a lower resistance, therefore excess of fibers will be deposited at that position. This phenomena must be regulated by time and length scales that are strongly connected to the dewatering flow, to the properties of the fibers and to the geometry of the fabric. However, systematic studies which could help exploiting this effect have not been performed.

Indeed, people have observed a strong influence of the forming wire on the final sheet. Adanur (1994) reported considerable influence of wire design on paper properties in laboratory forming, although the author did not report the characteristic of the pulp.

Herzig & Johnson (1999) experimentally showed that there are strong correlations between the forming wire and the surface layer of paper. Similar results have been obtained by Jong *et al.* (1999).

Furthermore, Hampson (1998) pointed out that the mesh size of the forming wire has to be chosen with consideration of the fiber-length distribution.

All these observations confirm two main ideas:

- There are physical mechanisms taking place in the initial dewatering that can modify the initial distribution of fibers (*i.e.* the distribution generated in the headbox and in the jet).
- There are a number of parameters (fiber length, mesh size, dewatering velocity, etc.) that are important in determining the change of the original fiber distribution (and therefore on the formation of the paper).

However, none of the authors above have analyzed in details the physical mechanisms involved in this process, therefore it is difficult to generalize the conclusions.

1.1.5. *Dynamics of network formation*

In order to understand what affects the distribution of fibers in a suspension, we can assume that the fibers are following the flow (*i.e.* low particle inertia). From this assumption, we can immediately conclude that relative motion between the fibers can only exist if the flow is not uniform. This means that a change in the fiber distribution has to be directly related to velocity gradients in the carrier fluid.

Velocity gradients are generated both by the interaction with an external body (boundaries like walls, forming wire and fiber network), and by the internal structure of the suspension (*i.e.* by the fiber distribution itself).

Due to the complexity of the system, it is very difficult to construct a deterministic model of this type of fiber suspension flow, where by deterministic model we mean a model that describes the motion of every single fiber in the suspension.

One interesting approach is to represent the formation of the fiber network as a stochastic process. Scharcanski & Dodson (1996*a*) followed this approach considering as stochastic variables the gaps between adjacent fibers in a one-dimensional model. Their aim was to compute the evolution of the initial distribution by modeling the influence of various phenomena which happen during the dewatering:

- Tendency of the fibers to form clusters (*flocculation*) or to be re-dispersed (*deflocculation*).
- Turbulence of the fluid phase.
- Regular localized drainage points due to the forming fabric.

Scharcanski & Dodson (1996*b*) model the change of the distribution function due to each of the above phenomena according to observations made on the shape of the distribution function, rather than on the real hydrodynamic interactions that actually drive the relative motion of the fibers in the suspension. This simple model is very instructive because it illustrates the physical phenomena that control the dynamics of network formation, however, to model them, they introduce unknown constants, which makes it impossible to do *a priori* predictions.

In order to gain a better understanding on the the mechanisms through which the hydrodynamic interactions modify the fiber distribution, we shall look at more detailed studies in the field of fiber suspensions.

1.2. Fiber suspension: physics and modeling

A complete description of all possible couplings between a liquid phase and solid, dispersed particles, in every possible condition, is extremely complicated.

Following Guazzelli (2006), the complexity arises from "the long range nature of the multi-body interactions between particles". Moreover, the macroscopic properties of the suspension are strongly dependent on the microstructure, defined as the relative position between the particles, which, itself, depends on the macroscopic properties.

In fiber suspensions, the elongation of the suspended particles introduces the additional complication of the orientation dependence of the hydrodynamic forces acting on them.

However, as pointed out by Petrie (1999), to understand the behavior of fiber suspensions it is essential to know first how a single fiber behaves

1.2.1. *Single fiber motion*

From the equations of motion of fluids in the limit of zero inertia (which approximates systems characterized by small scales and/or slow motion), one can calculate the force acting on a fiber subjected to a uniform background flow, and from that, calculate the velocity with which a fiber would sediment in a liquid, under the action of gravity.

This sedimentation velocity (often referred to as *Stokes velocity*) is orientation dependent, but, for each orientation, it eventually converges to a steady value. However, an important difference with respect to a sphere, is that a fiber can have a considerable motion perpendicular to gravity.

Another interesting observation one can make analyzing the solution to the equations of motion is that the perturbations introduced by the particles decay as $1/r$, where r is the distance from the particle centerline. This slow decay is responsible for the long range interactions mentioned before. The long range interactions, combined with the possibility of the fibers to move horizontally, will imply dramatic consequences when we will consider a population of fibers instead of only one.

If instead a non-uniform background flow is imposed, rod-like particle behaves very differently. For example, we can easily guess that in simple-shear flow, particles such as fibers will start to rotate. Indeed this was found by Jeffery (1922), who obtained the analytical solution for the motion of an isolated ellipsoid subjected to simple shear flow with no inertia. According to Jeffery's solution, which is in agreement with many experimental observations, an ellipsoid will move periodically in an orbit that depends only on the initial orientation, spending most of the time in the flow-vorticity plane. This means that, if one can neglect the inertia, a single fiber in a linear shear flow never forgets the initial conditions.

1.2.2. *Dilute and semi-dilute regime*

In contrast, a population of fibers in a suspension do forget the initial conditions and reach a statistical steady state. Effects like fiber-fiber contacts, elastic instability of the fibers, non-uniformity of the flow field (*i.e.* deviations from simple shear-flow), strongly affect the speed of the memory loss, thus modifying the orbit constants (see Stover *et al.* (1992), Zirnsak *et al.* (1994) and Becker & Shelley (2001)).

However the loss of memory can also be attributed simply to hydrodynamic interactions between the fibers. Therefore it is important to find a parameter that measure the extent to which fibers interact with each other in a suspension.

To begin with, we can define the volume fraction ϕ of the fiber phase as:

$$\phi = \frac{\pi}{2} n l d^2 \tag{1.2}$$

where, l is the fiber length, d is the fiber diameter and n the number density (number of fibers per volume unit).

Furthermore, we can define the fiber aspect ratio r as:

$$r = l/d.$$

Based on the value of the volume fraction and of the aspect ratio, we can estimate to what extent the fibers interact with each other. The interactions

between fibers depend on the concentration measure $N = nl^3$. This is the average number of fibers in a volume defined by the fiber length. Looking at equation 1.2, we can express N in terms of the volume concentration:

$$N = \phi r^2. \tag{1.3}$$

Now we can assume that for $N \ll 1$ the interactions between the fibers will be very weak. This regime is called *dilute regime*. From $N \ll 1$ it follows that $\phi \ll r^{-2}$, thus the volume concentration at we have a dilute suspension depends strongly on the elongation of the fibers. In particular, a suspension of long fibers will depart from the dilute regime at a much lower concentration than a suspension of short fibers.

Instead, for $r^{-2} \leq \phi \leq r^{-1}$, the fibers can still move freely but the hydrodynamic interactions cannot be neglected anymore. This is known as *semi-dilute* regime.

1.2.3. *Fiber orientation*

In the dilute regime we can describe the orientation distribution of a population of fibers by assuming that each fiber will behave as an isolated fiber that follows Jeffery's equation. Note that $N \ll 1$ is only a necessary condition for this model to be valid. The other required conditions are:

- The fiber length has to be smaller than any other flow scale (constant shear-flow).
- The aspect ratio r has to be uniform
- Inertia and body forces can be neglected
- The suspending fluid is Newtonian and incompressible

Under these assumptions, the Fokker-Planck equation together with Jeffery's relations for the rotational velocities can be used to describe the evolution of the probability density function ψ of the orientation of a population of fibers. The Fokker-Planck equation has the form:

$$\frac{D\psi}{Dt} + \nabla \cdot (\psi \dot{R}) = 0 \tag{1.4}$$

where $\dot{R}$ is the time derivative of the orientation vector of the particles in the given flow (for ellipsoids this derivative is given by Jeffery's solution). Equation 1.4 can be extended to include the effect of Brownian motion (Brenner (1974)). The Brownian motion introduces a diffusive term in (1.4), and it has the effect of smoothing out the orientation distribution, preventing the oscillatory solution when a steady shear stress is imposed.

The equation can be solved in closed form in the case of uniaxial and planar extension but not for shear flow. In the latter and in other more complicated cases, models of the higer order moments of the orientation distribution are needed (a closure problem similar to that of turbulence). Thus, in many cases, the Fokker-Planck equation has to be solved numerically.

Attempts of modeling the effect of weak inter-particle interactions or isotropic turbulence in the limits of the dilute regime have also been done. In particular, these effects have been modeled through a diffusive term introduced in the equation (similar to the way Brownian motion is treated). Doi & Edwards (1978) introduced a modified rotary diffusivity coefficient, which is dependent on the volume concentration and the orientation distribution itself. Among others, Olson & Kerekes (1998) and Shin & Koch (2005) studied the effect of the ratio between fibers and turbulent length scales on the rotary diffusivity coefficient. Recently Brown *et al.* (2006) and Hyensjö & Dahlkild (2008) have correlated experimentally and numerically the diffusivity coefficient to turbulent properties in a plane contraction modeling a paper machine headbox.

Being able to model suspensions that are semi-dilute or dense is very important since most of the practical applications exceed it. This is also the case of papermaking. However, this introduces complications that the previously mentioned studies only partly overcome.

1.2.4. *Numerical modeling, sedimentation and flocculation*

The most common approach to numerical modeling of fiber suspensions is to approximate the fibers with their centerline (known as *slender body theory*, see Keller & Rubinow (1975) and Cox (1970)) and locally distribute the solution for isolated spheres (stokeslet and doublets), and account for non-local interactions. In this way it is possible to account for non local interactions, so that in principle, any regime can be studied. However, as the fiber concentration increases, this approach quickly becomes computationally expensive.

Nevertheless recently, thanks to the increasing computational power, simulations of a relatively large number of both rigid and flexible fibers could be performed (see Tornberg (2004) and Tornberg & Gustavsson (2006)).

Although in this work the boundary conditions were periodic in all directions, so that quantitative comparison with the experiments is not possible, the results were in qualitative agreement with the experimental observations. In both the simulations and the experiments, fibers tend to form agglomerations with higher settling velocity (see Herzhaft & Guazzelli (1999) and Guazzelli (2001)).

The instability of settling homogeneous spheroids was predicted by Koch & Shaqfeh (1989), who explained that the origin of the instability is in the coupling between the orientation distribution and the velocity of the center of mass.

Fiber flocculation is an additional complication in the study of fiber suspensions which opens up to a number of still unanswered questions: even for a simple problem, such as the sedimentation of homogeneous fiber suspensions, at present, there are no theoretical predictions neither on the mean terminal settling velocity, nor a length scaling for the spatial velocity correlations.

1.2.5. *Fiber accumulation: the continuum approach*

In some cases, when N from equation (1.3) is large, the disperse phase can be considered as a continuum.

In this case, an Eulerian volume-averaged two-phase flow equation can be used to describe the evolution of the local volume fraction of fibers. This approach has been widely used in the field called *thickening theory*, where the initial concentration of fibers is high (*e.g.* $N > 20$), and in general the driving force is gravity (see for example Enwald *et al.* (1996)). For an extensive review on this field, see Concha & Bürger (2002).

If the initial concentration is lower, and the network is formed under the action of a filtration pressure (*Filtration theory*), the latter has to be implemented in the equation. This was done by Bürger *et al.* (2001).

The Eulerian volume-average equation is a very useful approach if one is interested in the average volume fraction, but it implies the assumption of uniform distribution along horizontal lines. Hence any information on the local variations in the planes perpendicular to the filtration velocity is lost, thus it is not useful to understand the dynamics that leads to local variations in the fiber network.

1.3. Flow measurements in multiphase flows

Since this work is essentially experimental, this introduction continues with an overlook of flow measurements in multiphase flow.

A fluid system becomes a multiphase flow when two or more phases are present. Examples are typically suspensions of gas bubbles in a liquid, emulsions, solids fluidized by a gas, or, like in our case, solids suspended in a fluid. For such flows, the quantities of interest are the concentrations and the velocities of the different phases, and these measurements are in general much more complicated to perform than in the case of single-phase flow. This is because, the extra phases often preclude optical access to the regions of interest. In the case of fiber suspensions, for example, fibers are generally not transparent and even at low concentrations, the optical access is very limited. This is a problem since many measurement techniques such as Particle Image Velocimetry (PIV), Particle Tracking Velocimetry (PTV), or Laser Doppler Velocimetry (LDV), widely used in single-phase flows are based on the physical principle of detecting an optical signal (*i.e.* scattered light) coming from tracer particles inserted in the flow. Therefore it is difficult, where not impossible, to apply them in flows where the optical access to the points of interest is hindered.

Other well established techniques like hot wire anemometry, instead, are not applicable due to the presence of a solid phase.

1.3.1. *Non-optical methods*

To overcome the limitations of the optical techniques, more sophisticated measurements systems have been developed. Most of them come from medical applications: Magnetic Resonance Imaging (MRI), Nuclear Magnetic Resonance (NMR), Positron Emission Tomography (PET), Electrical Impedance Tomography (EIT), x-ray radiography. The main advantage of these techniques is that they can be applied to a very broad range of concentrations, since they do not measure an optical signal and are non intrusive. For these reasons they have been extensively used for concentration measurements of complex flows *e.g.* by Turney *et al.* (1995), Etuke & Bonnecaze (1998), Young *et al.* (2006). The work of Seymour *et al.* (1993) shows the capability of MRI and NMR to measure velocity profiles as well.

The drawback of these techniques is that they require highly specialized users, they involve expensive equipments and they often impose limitations on the geometry of the experimental apparatus.

A less expensive and relatively simpler alternative is the Ultrasonic Pulsed Doppler Velocimetry (UPDV). This technique uses the doppler shift of an ultrasound wave to detect the position and the speed of a particle, and this makes it suitable for both concentration and velocity measurements of solid particles in solid-liquid suspensions, fluidized beds, or even three-phase gas-solid-liquid systems (see Wang *et al.* (2003)). The main limitation of UPDV is that the direction of the flow must be known *a priori*, since the outcome of the measurements depends on the angle between the flow and the probe.

Powell (2008) provides an excellent review over all the techniques mentioned above.

1.3.2. *PIV in multiphase flows*

Although this implies some complications, for flows where the disperse phases are not too concentrated and/or transparent, it is still possible to use techniques like the aforementioned PIV, PTV or LDV for velocity measurements.

In particular, measurements performed with PIV or PTV contain much more information than what can be extracted from LDV measurements. Thus we turn our attention to the first two methods.

PIV and PTV are based on similar procedures: after seeding the flow with tracer particles, images of the light scattered from the particles are captured in the region of interest at a known rate (usually a high speed camera is required). From the images, the displacement of the tracer particles, which is assumed to be equal to the flow velocity, can be calculated. To measure the velocity of the disperse phase, the tracers are the particles themselves (fibers, bubbles, etc.), whereas for the fluid phase, one needs to seed the flow with specific particles (generally very small), which are assumed to follow the dynamics of the fluid.

In PTV the density of the tracer particles is so low that it is possible to detect the displacement of the single particles, whereas PIV uses an Eulerian approach, measuring the average velocity of the seeding particles in a given area using cross-correlation techniques or similar.

The advantage of PIV is that it gives a spatially resolved velocity field over the entire (seeded) domain, however, if the flow is made of more than one (not invisible) phase, the velocities measured through cross correlations are the average velocities of the different phases.

There are several methods to overcome this problem. Delnoij *et al.* (1999) discriminated the liquid and gas phase in a bubble column by the different signals they generate in the correlation plane. As a fact the authors were using the knowledge that, in this particular case, due to the large density difference, the velocity of the gas will always be higher than the liquid.

In general, this approach is not possible because it requires prior knowledge of the flow field. Alternatively, digital image processing offers the possibility to post-process the images and to isolate the two phases into individual images, so that PIV can be applied only on the single phases. This is the approach used by Chung *et al.* (2007), who measured separately the liquid and the gas phase in a stirred vessel. To distinguish the in and out of plane bubbles they used a fluorescent dye in the fluid.

This second approach is more suitable for fiber suspension flows, since the density difference is very limited and in most cases the velocity of the fibers is very close to that of the carrier fluid.

Index of refraction matching and PTV for fiber tracking have been widely used for the study of dilute fiber suspensions, in particular to extract mean and fluctuating velocities and orientation of sedimenting fibers (see Herzhaft & Guazzelli (1999)), or to measure the orientation in shear flow near a solid wall (Carlsson *et al.* (2007)). In these studies, particle tracking was used to determine the motion and the orientation of the solid phase, but not (or in a very limited way) to study the velocity field of the fluid phase.

Holm (2005) used PIV to detect flow structure during fiber sedimentation, but he used dyed fibers as tracer particles in an index of refraction matched suspension, and therefore the results are only qualitative.

1.4. Present work

From what we have said we can conclude that, if one is interested in the evolution of the microstructure of a semi-dilute suspension in complex flows (such as the dewatering in papermaking), experiments are vital, since direct simulations are too expensive and a complete theoretical analysis too complicated. Experimental observations are also important for verification of computational models.

We have seen that there are at least two concurrent contributions to the dynamics of the fibers during the filtration: on one hand, under the action of gravity fibers tend to agglomerate in flocs; on the other hand they are transported by the filtration flow, and their relative motion is determined by the local velocity gradients. Therefore, both understanding of the fundamentals of fiber sedimentation and characterization of the filtration flow is needed.

In literature there are many experimental and theoretical works aimed at describing fiber sedimentation, however, despite the relevance for papermaking and other industrial applications very few extensive investigations have been made on the flow generated during the filtration of a fiber suspension.

One of the reasons is the difficulty of measuring in a time dependent two phase flow.

In this work, we tried to overcome this by combining index of refraction techniques, digital image processing and PIV. The details of the measurements techniques we have used, governing equations and scaling parameters, and the results of the measurements can be found in this thesis.

The structure of the thesis is the following: in chapter 2 we shall discuss the governing equations and the non-dimensional parameters that can be derived from them. The experimental apparatus is described in chapter 3. In chapter 4 we present the measurement techniques and in chapter 5 we show the results of the experiments, which are discussed in chapter 6. Finally, the conclusions are summarized in chapter 7.

CHAPTER 2

Governing equations and scaling

2.1. Problem formulation

The problem we want to address is sketched in figure (2.1). We have a vessel with impervious walls, which contains a dilute suspension of fibers.

In this configuration, a piston exerts a suction in such a way that the suspension is forced to flow through a semi-permeable mesh. The latter allows the fluid to pass while retaining the solid particles, obtaining the filtration of the suspension.

The suspension is semi-dilute (as defined in section 1.2.2) and both gravity and flocculation are present. In the scaling analysis, we do not consider the effects of the walls and of the free surface. Under these conditions, we are interested in how the suspension microstructure evolves during the filtration process due to the flow, which will be measured later.

Assuming that the fibers follow the fluid we can say that the system described above is equivalent to a system in which the mesh is moving in a steady suspension. This way we can easily show that the relative velocity between the centerline of a particle and the mesh V, can be decomposed according to:

$$V = V_m + v_s + v_c, \tag{2.1}$$

where V_m is the known velocity of the mesh (the imposed dewatering velocity in the original system), v_s is the settling velocity of the particle, and v_c is the velocity perturbation, where for perturbation we mean any deviation from the undisturbed uniform freestream conditions (see figure 2.2).

The settling velocity of a single fiber depends on the orientation of the fiber and we can calculate it from the solution of the Stokes equation (see section 2.3.2). In addition to isolated fibers, semi-dilute suspensions we can have agglomerates of fibers with higher settling velocities, as discussed in the previous chapter. There is no theoretical description of the settling velocity of a floc, but as a first estimation their velocity can be assumed to be in the same order of magnitude as that of the single fibers (see section 2.3.3a for a more detailed discussion).

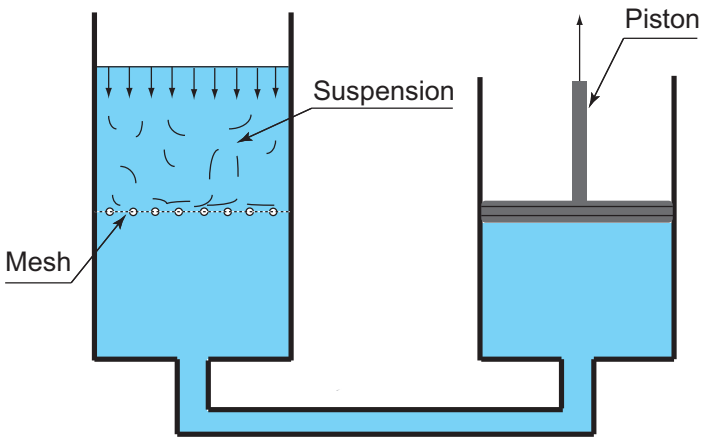

FIGURE 2.1. Schematic of the filtration problem. The channel to the left contains the fiber suspension and the screen through which the suspension is filtered. The piston controls the motion so that a constant flow rate is obtained in the main channel.

The perturbation v_c is introduced both by the interaction of the flow with the mesh, growing fiber network and by the sedimentation of the fibers and the flocs.

It is well known that in subsonic flow any perturbation is propagated over the entire domain, however we can assume that, in practice, the perturbation introduced by the mesh extends over a finite distance. We call this distance y_b and the region will be referred to as *boundary region*. Outside this region the fibers, due to gravity, can sediment in an initially quiescent fluid, and the perturbations in this region are only introduced by the sedimentation of the fibers.

The time t_s during which a fiber initially located at a distance y_0 from the screen experience free sedimentation is expressed by:

$$t_s(y_0) = \frac{y_0 - y_b}{V_m + v_s}. \tag{2.2}$$

From t_s, we can define a *free fall region* as the region in which the particles have had the time to settle for at least one fiber diameter d_p. The upper boundary of this region is given by the free surface, whereas the lower boundary

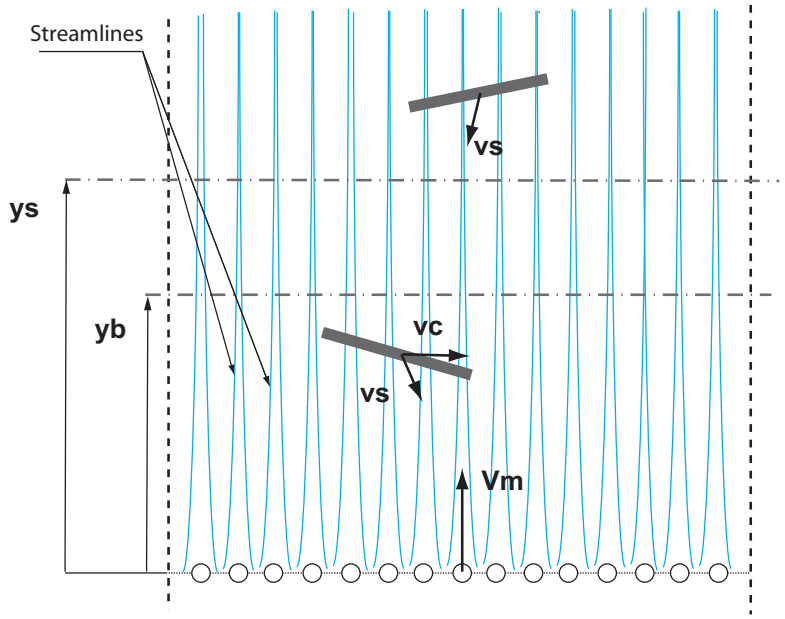

FIGURE 2.2. Schematic of the the problem. V_m is the velocity of the screen, v_s is the sedimentation velocity of each fiber, and v_c is a velocity perturbation. The concept of *boundary region* (y_b) and *free fall region* (y_s) is also shown.

y_s is given implicitly by the definition of free fall region:

$$t_s(y_s) = \frac{y_s - y_b}{V_m + v_s} = \frac{d_p}{v_s}. \tag{2.3}$$

This gives:

$$y_s = y_b + d_p(1 + \frac{V_m}{v_s}). \tag{2.4}$$

Furthermore, we can derive a second time scale, which represents the residence time of a particle in the boundary region:

$$t_b = \frac{y_b}{V_m + v_s}. \tag{2.5}$$

The free-fall region above y_s and the boundary region below y_b can be treated separately. The evolution of the suspension in the free fall region can be described by the results form the sedimentation studies, whereas the boundary region needs a more complicated approach, involving Jeffery orbits and the Fokker-Planck equations.

2.2. Governing equations

In this section we shall discuss the equations for both the liquid and the solid phase, to provide a physical background which helps to interpret the results as well as to derive the scaling parameters.

2.2.1. *Fluid phase*

The governing equation of motion of a fluid can be derived from the law of momentum conservation (*Newtons second law*), and expressed as:

$$\rho\frac{\partial \mathbf{u}}{\partial t} + \mathbf{u}\cdot\nabla\mathbf{u} = -\nabla p + \rho\mathbf{g} + \nabla\cdot\tau. \tag{2.6}$$

This is a non-linear partial differential equation, where $\mathbf{u}$ and p are the instantaneous velocity and pressure fields, ρ is the density, $\mathbf{g}$ is the gravity field and τ is the stress tensor. The terms on the left-hand side of the equations are the inertial terms, responsible for the non linearity of the equation. The right-hand side contains the forces applied to a fluid element.

In this vector equation there are 11 unknowns, given by the three velocity components, the pressure, the density and the six elements of the symmetric stress tensor. For a Newtonian fluid, the stress tensor is proportional to the strain rate, thus equation 2.6 becomes:

$$\rho\frac{\partial \mathbf{u}}{\partial t} + \mathbf{u}\cdot\nabla\mathbf{u} = -\nabla p + \rho\mathbf{g} + \mu\nabla^2\mathbf{u}, \tag{2.7}$$

where the constant of proportionality μ is the dynamic viscosity of the fluid. Equation (2.7) is known as *Navier-Stokes* equation, from the names of the two scientists who independently derived it, more than 100 years ago.

In this form, the unknowns are reduced to 4, and thus, one more equation is needed. This is given by the law of conservation of mass, which, for incompressible fluids reduces to:

$$\nabla\cdot\mathbf{u} = 0. \tag{2.8}$$

2.3. Boundary conditions

In order to solve this system of equations, we need to set appropriate boundary conditions. These conditions depend on the specific case we are taking into account. The most common case is the solid-liquid interface, since in general, the flow is bounded by solid walls. In this case the condition is:

$$\mathbf{u} = \mathbf{u}_{wall}. \tag{2.9}$$

This is usually referred to as the *no-slip condition*.

It is possible to set inlet or outlet boundary conditions. In that case, the velocity and the pressure field has to be known at every point of the boundary.

Liquid-liquid or liquid-gas interfaces can also be described, but they require more complicated conditions, which we shall not discuss in this thesis.

With the boundary conditions, the system of equations 2.6 and 2.8 is properly defined. However, for most practical applications the analytical solution is not available. In these cases the full problem can be solved numerically, or, to get estimations of the flow behavior, simplified solutions can be sought for.

It has to be pointed out that this set of equations has been derived for Newtonian fluids. It is well known that adding a dispersed solid phase can modify this behavior and make the suspension non-Newtonian (*i.e.* non-linear relation between stress and strain-rate).

This is because part of the momentum is transfered to the particles, which in turns yield additional stresses in the fluid. These stresses depend on the particular conformation of the solid phase (*i.e.* on the microstructure), and the determination of a constitutive relation between the two, is a very broad subject named *rheology*[1]. A detailed discussion on stresses produced by non-spherical particles in a fluid can be found in Batchelor (1970).

2.3.1. *Non-dimensional Navier-Stokes equations*

In order to find the minimum number of flow parameters that regulate the flow behavior, we can rewrite the equations in a non-dimensional form. We do this by scaling each variable with constant reference properties, such as characteristic velocity, length and time scale, or reference values for pressure or density.

Scaling velocity with a velocity scale U, lengths with a length scale L, and pressure with ρU^2, equations (2.8) and (2.7) become:

$$\nabla' \cdot \mathbf{u}' = 0 \tag{2.10}$$

$$\frac{D\mathbf{u}'}{Dt'} = -\nabla' p' + \frac{1}{\mathrm{Re}} \nabla'^2 \mathbf{u}' \tag{2.11}$$

where Re is the Reynolds number defined as $\mathrm{Re} = \rho U L/\mu$. As we can see, Re is the only remaining parameter.

Looking at equation (2.11) in this form is very useful, because, based on the value of Re, we can have an estimation of the order of magnitude of the various terms.

At very high Reynolds numbers, the viscous term become small compared to the left-hand-side of the equation, meaning that inertial forces are dominant on the viscous forces.

[1]The word comes from the greek words *rheo*: flow, and *logos*: though, reason.

On the other end, if the Reynolds number goes to zero, the viscous term is dominant and the inertial term can be neglected. This eliminates the non linear terms of the equation, providing an enormous simplification.

Looking at the definition of Re, this limit is reached either when we have a highly viscous fluid, or when the characteristic velocity or length scales are small.

The latter often occurs in fiber suspension flows for the flow around the fibers, given the small size of the particles. In the next section we shall see how this hypothesis can simplify the study of this type of flows.

2.3.2. *Solid phase*

2.3.3. *Generalities*

The constitutive relation for the additional stresses mentioned above can only describe the macroscopic behavior of a suspension. However if we are interested in the suspension microstructure (*i.e.* on the evolution of position, orientation and velocity of each individual particle), this approach cannot provide enough information.

In general, the complete evolution of the microstructure can only be achieved by solving the full Navier-Stokes equations with appropriate boundary conditions, coupled with the momentum equations for the particles. This yields forces and torques that determine the motion of the particles and the additional stresses on the fluid.

Due to the non linearity of the Navier-Stokes equations, this approach requires unreasonable computational times, which makes it impossible to use it for complex systems. In particular, it would be too costly to use it for the study of non-spherical particles (like fibers), due to the additional degrees of freedom which one has to account for.

However, for most of the practical applications, particles are so small that the Reynolds number based on the particle diameter is smaller than one. This in turns mean that hydrodynamic forces and torques can be calculated from the Navier-Stokes equations simplified as discussed in the previous section. Hence, the flow around a small particle (*i.e.* $\mathrm{Re} \ll 1$) is described by:

$$\nabla p \approx \nabla^2 \mathbf{u} \tag{2.12}$$

With an equal sign, valid or Re=0, equation (2.12) is known as *Stokes equation*[2]. What makes it so appealing is that it is a linear partial differential equation and thus yields many solutions in closed form. The resulting flow is referred to as *creeping flow*.

One of the uses one can make of the Stokes equation is to compute the flow around an immersed body. Stokes himself calculated an analytical solution for

[2]George Gabriel Stokes (1819-1903), who first developed this theory in 1851

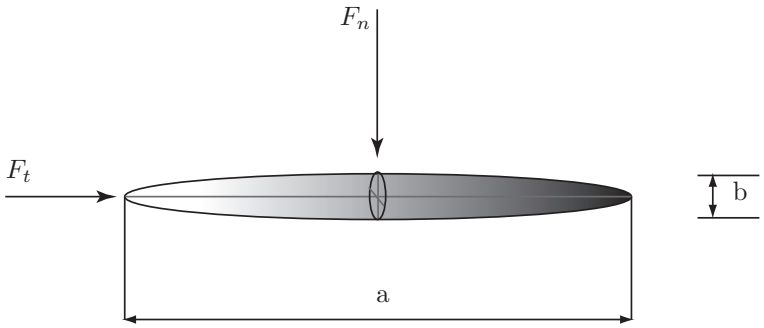

FIGURE 2.3. Prolate spheroid. Obtained by the rotation of an ellipse of axes a and b around the major axis. F_n and F_t are the components of the hydrodynamic force normal and perpendicular to the major axis, respectively.

the flow around a sphere in a uniform flow U. From this solution he expressed the drag as:

$$F = 6\pi\mu U a. \tag{2.13}$$

This expression says that the proper drag coefficient should be $F/\mu U a = 6\pi$, where a is the radius of the sphere. (Although everyone uses the inertia type of definition $C_d = 2F/\rho U^2$, which introduces a Reynolds number dependence that does not exist for three dimensional bodies!) For two dimensional bodies however, Stokes equation cannot be solved with the appropriate boundary conditions without including inertia (Stokes paradox). Oseen (1910) removed this paradox introducing a linearized convective acceleration to the momentum equation. Oseen's improvement introduces an asymmetry to the solution due to a wake behind the body (but not separation), and it can be applied to the flow around a sphere for small but finite Reynolds numbers.

Stokes sphere law (and Oseen improvement) has proven to be accurate for nearly spherical bodies as well, and it is has many practical applications, like the analysis of the motion of sand and dust particles.

Similar analysis can be performed for any three-dimensional body, provided that one has enough analytical skills.

A shape of interest for us is the prolate spheroid (see fig.2.3), since its elongated form resembles a fiber.

In this case the flow might be tangential or perpendicular to the long axis, but in both cases the drag force has the form:

$$F = C\mu U a \qquad C = const. \tag{2.14}$$

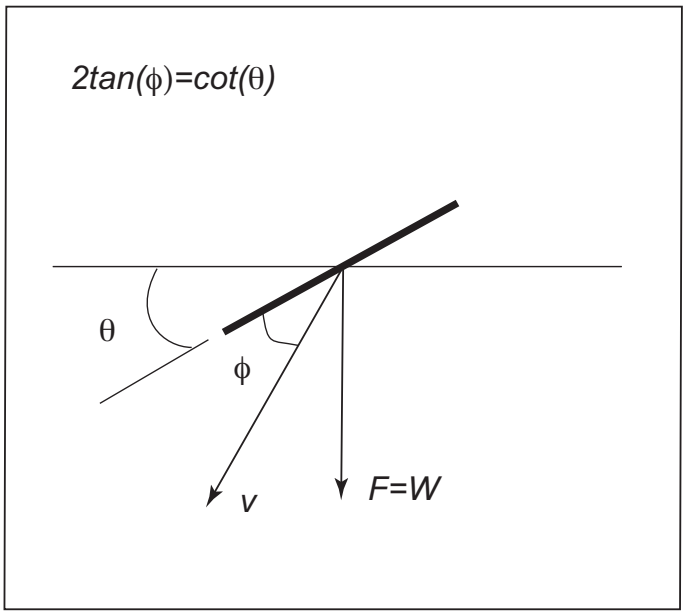

FIGURE 2.4. Isolated fiber subjected to body force W. Due to the linearity of of the Stokes equation, the two components of the force F_n and F_t can be superimposed and the direction ϕ of the sedimentation velocity v can be calculated as a function of the fiber orientation θ.

Analytical solutions for these coefficients exist, but are rather complicated expressions. Therefore it is more convenient to use curve-fit formulas like those provided by Clift *et al.* (1978), valid for the limit of $a \gg b$:

$$C_t \approx \frac{4\pi a/b}{ln(2a/b) - 0.5} \qquad C_n \approx 2C_t \tag{2.15}$$

2.3.3a. *Sedimentation.* With the help of the drag coefficients and of the slender body theory (valid in the limit of infinite aspect ratio), we can calculate the sedimentation velocity of an isolated fiber (see Mackaplow & Shaqfeh (1998)):

$$\begin{aligned} U_s = \frac{\Delta\rho(d)^2}{16\mu}[(\ln 2r + 0.193 + O(\ln 2r)^{-1})\mathbf{g} \\ + (\ln 2r - 1.807 + O(\ln 2r)^{-1})(\mathbf{p}\cdot\mathbf{g})\mathbf{p}] \end{aligned} \tag{2.16}$$

where r is the aspect ratio, $\mathbf{p}$ is the fiber orientation vector, and $\mathbf{g}$ is the gravity. Equation (2.16) clearly shows that the settling velocity of a fiber

depends on the orientation and that indeed fibers, unlike spheres, can have a motion perpendicular to gravity (see figure 2.4).

According to the linear stability analysis of Koch & Shaqfeh (1989), it is this coupling of the velocity and the orientation that causes the instability due to which fibers tend to agglomerate in flocs. Agglomeration in flocs have been detected experimentally by *e.g.* Herzhaft & Guazzelli (1999). According to this work, the average velocity of sedimenting fibers in dilute and semi-dilute suspensions reaches a steady value, which, in the case of dilute suspensions, can be higher than the maximum settling speed of an isolated fiber.

It has to be said that the steady-state settling velocity is still an open issue since it is confirmed by some numerical simulations like those of Butler & Shaqfeh (2002), but it is contradicted by the work of Mackaplow & Shaqfeh (1998). Furthermore, if the steady state velocity really exists, Herzhaft & Guazzelli (1999) did not find any scaling law for it.

As a rough estimation, however, one can say that in all the investigated cases, the average settling velocity, although with large fluctuations in the case of semi-dilute suspension, has always been of the same order of magnitude as the maximum Stokes velocity (2.16) of an isolated fiber. This has been confirmed by a recent experiment of Metzger *et al.* (2007).

2.3.3b. *Simple shear flow.* Jeffery (1922) derived an extremely useful analytical solution of the Stokes equation. He solved the equation of motion of a single ellipsoid in simple shear flow. For the case of the flow around the spheroid defined in figure 2.3, of aspect ratio $r = a/b$ subjected to the constant shear rate $\dot{\gamma}$, Jeffery's solution is:

$$\dot{\phi} = -\tfrac{\dot{\gamma}}{r^2+1}(r^2 \sin^2\phi + \cos^2\phi) \tag{2.17}$$

$$\dot{\theta} = (\tfrac{r^2-1}{r^2+1})\tfrac{\dot{\gamma}}{4}\sin 2\phi \sin 2\theta \tag{2.18}$$

with ϕ and θ defined in fig. 2.5.

Thus the rotation rates $\dot{\phi}$ and $\dot{\theta}$ depend linearly on the shear-rate.

Moreover, from (2.17) and (2.18) we can derive the period of rotation:

$$T = \frac{2\pi}{\dot{\gamma}}\left(\frac{r+1}{r}\right), \tag{2.19}$$

which surprisingly says that particle with for higher aspect ratio will take longer time than for shorter fibers to perform one orbit . This can be explained if we look at the rotation rates, for which we can see that, although long fibers flip faster than short fibers, they spend more time aligned in the flow direction.

Furthermore, by integrating (2.17) and (2.18), we can obtain the particle trajectories:

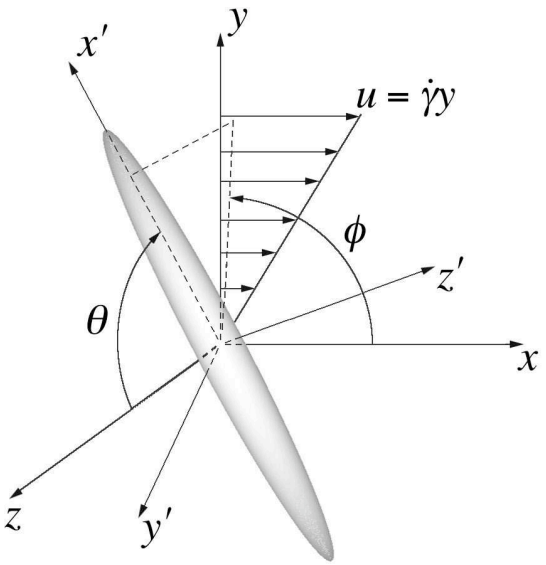

FIGURE 2.5

$$\cot\phi = -r\cot(\tfrac{2\pi t}{T} + \phi_0) \tag{2.20}$$

$$\tan\theta = \frac{Cr}{(r^2\sin^2\phi + \cos^2\phi)^{0.5}} \tag{2.21}$$

where C and ϕ_0 are constants that depend on the initial conditions. This means that a fiber subjected to shear flow performs a periodic elliptic orbit, which is completely determined by the initial conditions.

2.3.3c. *Dilute suspensions theory.* Although it has been shown that Jefferys theory is valid for any shape with fore-aft symmetry, and thus also for cylinders, we have to remember that it has been derived for an isolated fiber. Thus we have to be careful if we want to apply the theory to a population of fibers in a suspension.

This is because in a real suspension, fibers can forget the initial conditions and modify their orbit constants. As already mentioned in the introduction, this can happen not only in the case were considerable Brownian motion is present, but also due to other effects. For instance non-Brownian fibers can experience the drift due to hydrodynamic interactions, turbulent fluctuations, fiber flexibility or other flow non-homogeneities.

However, in case of dilute-suspensions (*i.e.* $N \ll 1$) where none of the effects mentioned before are important, we can deduce the behavior of the population by assuming that each fiber behaves as an isolated fiber, thus applying Jeffery's equations.

The study of the time evolution of the orientation distribution of a population of fibers can be done by using the Fokker-Planck equation (see eq.(1.4)). Under the assumptions of dilute regime (see 1.2.2), the rotation rate $\dot{R}$ can be derived from Jefferys solution for any linearly varying flow. Substituting (2.17) and (2.18) in (1.4), we obtain the Fokker-Planck equation for the case of simple shear flows:

$$\begin{aligned}\frac{D\psi}{Dt} = &\frac{1}{\sin\theta}\frac{\partial}{\partial\phi}\left[\frac{\dot{\gamma}}{r^2+1}(r^2\sin^2\phi+\cos^2\phi)\psi\right] \\ &-\frac{\partial}{\partial\phi}\left[(\frac{r^2-1}{r^2+1})\frac{\dot{\gamma}}{4}(\sin 2\phi\sin 2\theta)\psi\right].\end{aligned} \tag{2.22}$$

In the general case, $\dot{R}$ is obtained from the local strain rate and vorticity.

2.4. Phase-coupling equations

The momentum coupling equation between the liquid and the solid phase is:

$$F = \rho_p V_p \frac{dv}{dt} \tag{2.23}$$

where v is the translational and rotational velocity of the particle, ρ_p is the particle density, and V_p is the particle volume. F is the hydrodynamic force acting on the fiber. In the previous section it has been shown that in Stokes flow F has the form $F = C\mu d_p(u-v)$, where u is the velocity of the fluid, d_p is the particle diameter, and C is a coefficient that depends on the fiber orientation. Hence, equation 2.23 can be rewritten as:

$$\frac{dv}{dt} = \frac{C\mu}{\rho_p d_p^2}(u-v). \tag{2.24}$$

If we introduce $\tau_{v_t} = \rho_p d_p^2/C\mu$ the solution to equation 2.24 has the form:

$$v = u(1-e^{-t/\tau_{v_t}}). \tag{2.25}$$

As can be seen, τ_{v_t} is the response time of the particle, *i.e.* the time it takes for a particle to adjust to a change in speed of the carrier fluid. Note that this response time is dependent on the fiber orientation through the coefficient C.

In addition to the equation for the translation, one should consider also the equations for the rotation. In 3D, these equations are rather complicated. However in principle, given the momentum M from Jeffery's solution, the rotational response times τ_{v_r} can be calculated in a similar way as for τ_{v_t}.

2.5. Non-dimensional parameters

Given the complexity of the governing equations, it is useful to analyze the parameters that come out from a dimensional analysis.

- For the fluid phase, the parameter of interest is the Reynolds number $\mathrm{Re} = \rho UL/\mu$, which tells us whether inertial terms can or cannot be neglected.
- The relevant parameter that emerges from the equation of motion of the solid phase is the fiber aspect ratio $r = a/b$, which controls both the particle trajectory (in sedimentation) and the rotation rate (in shear flows).
- Another important non-dimensional number, known as *Stokes number*, can be extracted from the momentum coupling equations, and it is defined as:

$$St = \frac{\tau_v}{\tau_f} \tag{2.26}$$

It relates τ_v, the particle response time to τ_f, which is some characteristic time scale of the flow. Thus, if $St \ll 1$ the response time of the particle is small compared to a characteristic time of the flow, then the particle will follow the streamlines.

The relevant Stokes number for a sphere is only the one relative to the translational motion. For elongated bodies such as fibers, this will be orientation dependent. Furthermore, in the case of non spherical bodies one has to account for the additional degrees of freedom (*i.e.* those corresponding to the rotation) as well. This means that the dynamic response of a fiber will be determined by at least two Stokes numbers, St_t for translation and St_r for the rotation, whose order of magnitude can be estimated as:

$$St_t = \kappa \mathrm{Re}_{d_p} \tag{2.27}$$

$$St_r = \kappa \mathrm{Re}_{\dot{\gamma}} \tag{2.28}$$

In these equations $\kappa = \rho_p/\rho_f$ is the density ratio between fluid and fibers. Equation (2.27) is the translational Stokes number, where Re_{d_p} is the Reynolds number based on the fiber diameter and a characteristic velocity U. Equation (2.28) instead shows the rotational Stokes number, where $\mathrm{Re}_{\dot{\gamma}} = l^2\dot{\gamma}/\nu$ is the Reynolds number based on the shear rate $\dot{\gamma}$, where ν is the kinematic viscosity. In this work the Stokes numbers will be small since the particle Reynolds numbers are small and $\kappa \approx 1$.

2.6. Scaling

It is interesting to compare the scales provided by the equations with the scales of our problem.

	Min	Max
r	20	100
Re_{d_m}	4.5	13.6
Re_{d_p}	0.9	2.7
Se	$\ll 1$	$\ll 1$

TABLE 2.1. Values of the non-dimensional parameters on the typical operative conditions of a Fourdrinier paper machine.

The first parameter can be obtained by comparing the residence time of a particle in the boundary region (t_b, equation (2.5)) with the period of revolution of a fiber performing Jefferys orbits (T, equation (2.19)):

$$T_r = \frac{t_b}{T} \tag{2.29}$$

This parameter tells us to what extent the orientation distribution function will be affected in the boundary region.

A second parameter, which compares the height of the free-fall region to the height of the boundary region is obtained as:

$$H_s = \frac{H - y_s}{y_b} = (\frac{H}{y_b} - 1) - \frac{d_p}{y_b}(1 + \frac{V_m}{v_s}) \tag{2.30}$$

where H is the total height of the suspension. As before, y_b is the still unknown height of the boundary region, d_p is diameter of the fibers and V_m is the filtration velocity. Since the ratio between the sedimentation and the drainage speed appears in equation (2.30), we define it as a non-dimensional parameter Se, *i.e.*

$$Se = \frac{v_s}{V_m}. \tag{2.31}$$

The parameters T_r and H_s tell us which physical processes that take place during drainage. However, at this point y_b is not known.

2.7. Conditions in a paper machine

In order to compare the conditions in a paper machine with our experimental conditions, we report the values of the most relevant non-dimensional parameters for the operative conditions in a paper machine in table 2.1. The non-dimensional parameters are the fiber aspect ratio r, the Reynolds number based on wire diameter Re_{d_m}, the Reynolds number based on fiber diameter Re_{d_p} and the sedimentation number Se.

The values are calculated assuming the filtration velocity calculated in section 1.1.4.

CHAPTER 3

Experimental setup

3.1. Apparatus description

In order to study the filtration process of a semi-dilute suspension under the conditions illustrated in figure 2.2, an apparatus where these conditions can be experimentally reproduced has been designed and built.

Figure 3.1 shows a schematic of the experimental setup. The apparatus consist of a test section and a driving unit.

3.1.1. *Test section*

The test section is a vertical channel. The channel was built in Acrylic glass, which ensures optical access.

A woven screen is mounted across the section at half of the channel length, which is 700 mm in total. The wires of the screen have a diameter of 1 mm and the gaps are 2 mm wide. The gap size is small compared to the length of the fibers that will be used in the experiments, so that most of the fibers in the suspension will be retained on top of the screen, while the fluid is filtered through it.

The cross-section of the channel is 80x80 mm^2. The channel width has been chosen in such a way that the boundary layer developing at the wall does not reach the center of the section during the experiments. Therefore there is a region where the velocity profile is flat, and in that region the effect of the walls can be neglected. This will be verified in section section 5.2. The dimensions of the test section and the screen are summarized in table 3.1.

3.1.2. *Driving unit*

The driving unit is a piston-cylinder system that controls the flow rate in the test section. The flow rate is generated by the upward or downward motion of the piston, which aspires or pushes the fluid into the test section. The piston is driven by a DC-motor and its position is monitored with a linear position sensor.

The velocity of the piston, and therefore of the free surface in the test section, is controlled with the closed loop described in figure 3.2. Under our experimental conditions, the velocity of the piston was directly proportional to

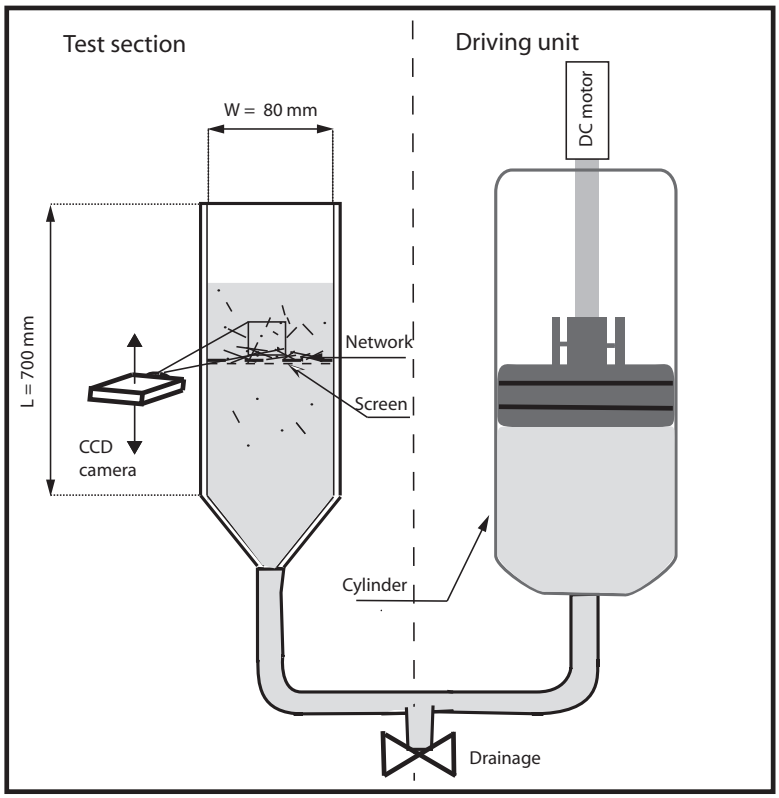

FIGURE 3.1. Experimental setup. The apparatus consists of a test section (left) and a driving unit (right).

the voltage $u(t)$, thus the loop allows us to control the velocity through the choice of the function $Vs(Ys)$.

The velocity of the piston can be related to the velocity the free surface of the test section by knowing the ratio between the area of the piston, A_p and the area of the channel A, which is $A_p/A = 4.9$.

3.1.3. *Light source*

The light source is a CW cold white light (Schott KL2500), focused into a light sheet with a cylindrical lens. The measurement plane is defined by this light sheet.

Test section:	
Cross-section	80×80 mm
Total channel length	700 mm
Length above the screen	350 mm

Screen properties:	
Wire diameter d_s	1 mm
Mesh width	2 mm

TABLE 3.1. Summary of test section and screen sizes.

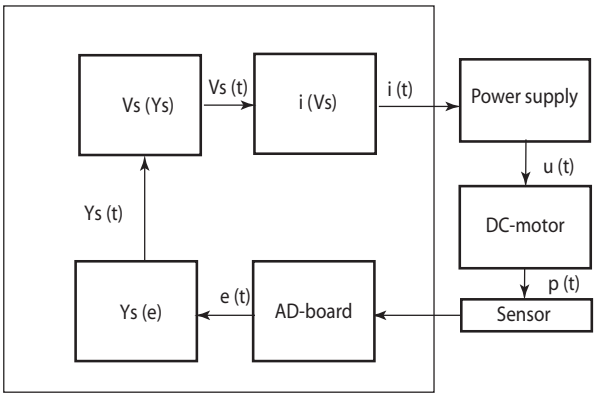

FIGURE 3.2. Velocity control loop. At each time interval the actual position of the piston is read through a linear position sensor. An AD board acquires the signal $e(t)$ which is transformed to the position of the free surface through the calibration curve $Ys(e)$. Successively an input signal $i(t)$ is generated according to the function $Vs(Ys)$. This goes into the power supply, which provides the voltage $u(t)$ to the DC motor.

3.1.4. *Camera and optics*

Images of the flow are captured with a CCD (Charged Coupled Device) digital camera Prosilica GE680. It has a resolution of 640×480 pixels and a maximum frame rate at full resolution of 200 fps. The lens that has been used has a focal length of 25 mm.

3.2. Fibers and fluid

The material used to produce the fibers is *Fluorocarbon*. This material was chosen for its transparency and flexibility, as well as for the large availability on the market: Fluorocarbon is available as a single filament winded in spools (typically used as a fishing line). In order to obtain fibers with the desired length from it, a controlled and repeatable cutting procedure is required. The procedure we followed to obtain our fibers is the following (see also figure 3.4):

(i) The Fluorocarbon filament is winded around a rod of 6 mm of diameter. The rod has two slits located diametrically opposite to each other. During the winding a tension to the filament is applied so that there is no gap between the spires.
(ii) After the winding, the filament is fixed at both ends of the rods in order to maintain the tension.
(iii) The rod is clamped along its entire length in a specially made device and cut with a scalpel along one (or both) slits so that one (or two) fiber(s) is obtained for each spire around the rod.
(iv) The rod is released from the clamp and the fibers are collected in a batch located underneath.

Depending on the number of cuts (one or two) fibers of length equal to or half the circumference of the rod can be obtained. The rod used in the present work gives $l = 9.4$ or 18.8 mm.

In order to determine the quality of the cut we inspected random samples of fibers with a microscope to investigate the shapes of the fiber ends. A typical image is shown in figure 3.3. From this visual inspection we concluded that the cutting produced very sharp ends and therefore the fibers have a cylindrical shape. The diameter of the fibers is specified by the manufacturer and it is $d = 0.26$ mm. The density was measured by putting a weighted amount of fibers in a graduated container with water where the variation of volume could be measured. The density was found to be $\rho_p = 1.8$ g/cm^3.

Another reason which led to the choice of Fluorocarbon is its relatively low index of refraction (IoR), nominally equal to 1.42. This is an important property because in order to perform the measurements, we need to make the suspension optically transparent, and therefore to match the IoR of fibers and suspending fluids. The IoR of 1.42 can be matched by a solution of 65% of glycerine in water, whereas most of the other plastic polymers (like Nylon), have IoR of about 1.47, which matches that of pure glycerine.

The viscosity of the 65% of glycerine solution is $\mu = 15$ cSt, only fifteen times larger than that of water, whereas the viscosity of pure glycerine is 1000 times larger than the viscosity of water. The advantage of using the former rather than the latter is that we can reach Reynolds numbers approaching those of papermaking.

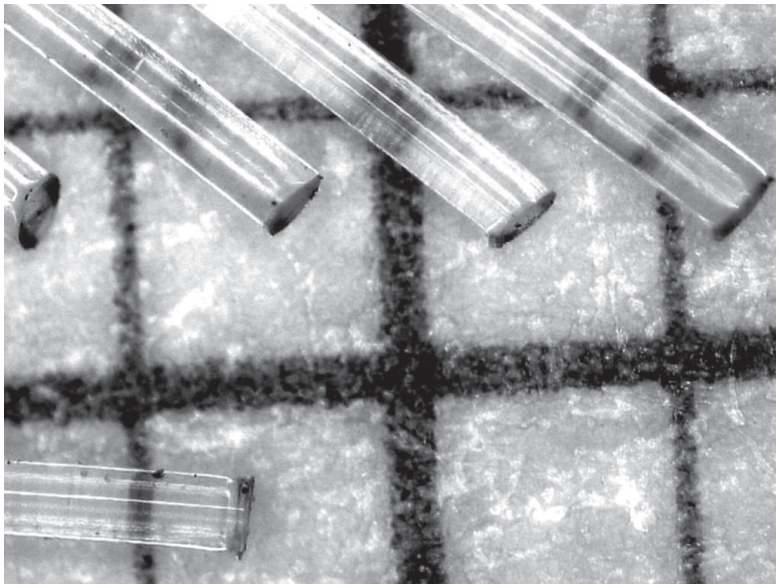

FIGURE 3.3. Microscope image of fiber ends. The graduated paper in the background gives an idea on the sizes. The distance between parallel lines is 1 mm.

However Fluorocarbon is characterized by a strong optical dispersion[1](see figure 3.5), which means that the index of refraction of the fiber changes with the color of the light. This makes it impossible to match the IoR of particles and fluid in white light. One solution to this problem would be to filter the light using a band-pass optical filter. However the filter drastically increases the power demand for the light source, and it was not always possible to use it with the combination of light sources and cameras at our disposition.

Geometrical and physical properties of fibers and fluid are summarized in table 3.2.

3.2.1. *Tracer particles*

The flow is visualized with Polyamid Seeding Particles (PSP) of 20 μm of diameter, from DANTEC.

[1]Dispersion is the phenomenon in which the phase velocity of a wave depends on its frequency.

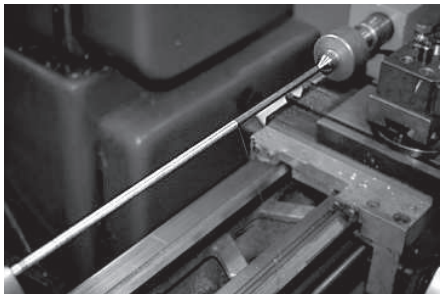

(a) Lathe used for the winding.

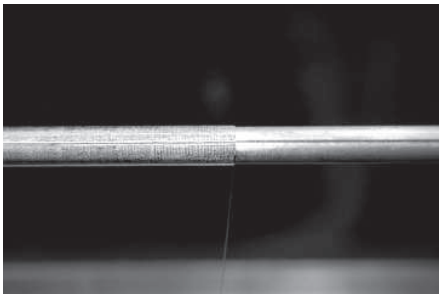

(b) Close up of the spires.

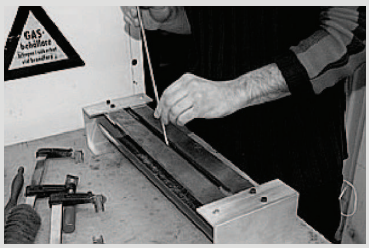

(c) Clamping device.

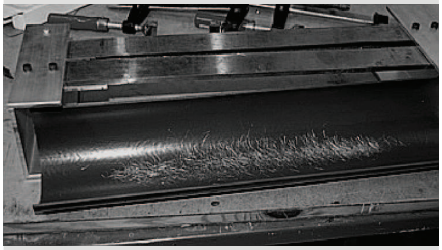

(d) Fibers after the cutting.

FIGURE 3.4. Cutting procedure.

Fluid properties (65% Glycerine-water):	
density ρ_f	1.17 g/cm^3
viscosity μ_f	1.51×10^{-2} Pas
IoR	1.42

Fibre properties:	
density ρ_p	1.8 g/cm^3
diameter d_p	0.26 mm
length l	9.4, 18.8 mm
IoR	1.41-1.43

TABLE 3.2. Fluid and fiber properties.

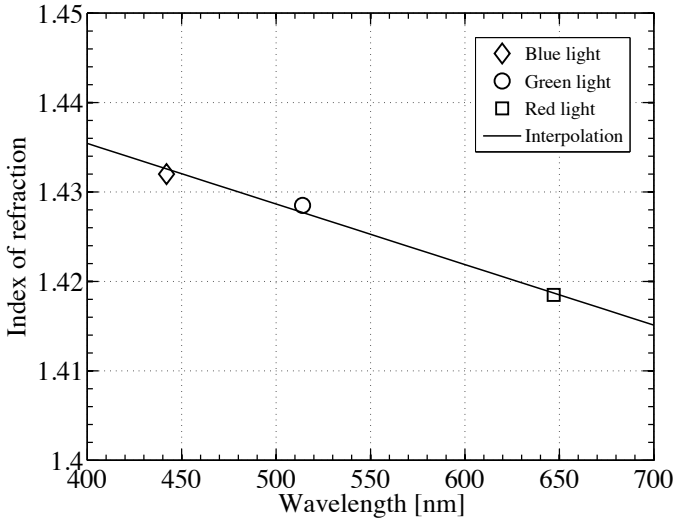

FIGURE 3.5. Index of refraction of the fibers. Measured by Dr. Göran Manneberg, associate professor at the department of Biomedical and X-ray physics of KTH, Sweden.

CHAPTER 4

Measurement techniques

We are interested in measuring the time resolved velocity field of the fluid phase during the filtration process in the experimental setup described in chapter 3.

This is done by (i) seeding the flow with small tracer particles, (ii) capturing images of the scattered light from the illuminated particles in the region of interest, (iii) processing the digital images to enhance the tracer particles and filter out the rest, (iv) measure the displacement of the tracer particles from one image to another, (v) from the displacements and the known time between the images, calculate the velocity field.

In the present chapter we shall discuss step (i),(ii),(iv) and (v), which are the key elements of Particle Image Velocimetry, and step (iii), an additional image processing stage.

4.1. Particle Image Velocimetry: a short review

Following Adrian (2005), PIV can be defined as a "quantitative measurement of fluid velocity at a large number of points".

As already mentioned, the method consists in seeding the flow with tracer particles, capturing images and calculating the velocity in the measuring plane from the displacements of the tracer particles.

The first of this type of measurements were achieved in the late 70s by several groups (See Barker & Fourney (1977), Dudderar & Simpkins (1977) and Grousson & Mallick (1977)). In their work, each frame was exposed two times within a short time interval so that each particle was recorded twice in a single frame. The displacement was calculated from the fringes created by the particles using the method of laser speckle. However, speckle patterns are created only at high particle density (where particle density is the number of particle per resolution volume), a condition that is not desirable for the study of the dynamics of most flows.

Consequently, the method evolved towards the use of lower particle density. In this case fringes are seldom formed and the image plane rather contains images of the individual particles. Hence, the term Particle Image Velocimetry was introduced to distinguish this mode of operation from the laser speckle technique (see Pickering & Halliwell (1984)).

4.1.1. *Illumination type and image recording techniques*

During the years many types of illumination, recording techniques and displacement evaluation methods have been used, and one can find dozens of papers describing different kind of flow-measuring systems based on optical imaging.

Starting with light sources, the main candidates are Continuous Wave (CW) lasers, pulsed lasers, CW white illumination with shuttered recording cameras and flash lamps. The choice of the light source depends on the type of flow we want to study, to the tracer particles we are using as well as to the recording device. In general, lasers provide a powerful source of monochromatic light, but imply high costs and strict safety rules. White light sources on the other hand, have low cost and are easy to use, but have a finite extension and are more difficult to collimate into a light sheet.

For image recording instead, the two foremost options are: double exposure on a single frame (as in the speckle technique), or single exposure on multiple frames. The former was mainly used in the early times because of the limited speed of the cameras, but it has two major disadvantages: ambiguity in the flow direction, and limited dynamical range (defined as the ratio between the highest and the lowest measurable velocity). In fact, in double exposure images, the minimum detectable displacement is limited by image overlapping (*i.e.* at very low speed the displacement is so small that the particles are indistinguishable). This reduces the dynamical range to unacceptable values (typically between 5 and 10). Both problems can be overcome by shifting the second image in such a way that the directional ambiguity is removed (see Adrian (1986)). This eliminates the problem of image overlapping as well, increasing the dynamic range to values between 100 and 200.

The problem is that image shifting requires a complicated mechanical system to move the camera precisely the desired amount, and now that technological developments have made the digital cameras fast and accurate enough to record the particles in two individual frames with single exposure, this complication has become obsolete. This is because in single exposure images the direction is determined by the temporal order of the pictures and the image overlapping for small displacements is completely eliminated. Therefore, double frame, single exposure recording has become the predominant technique.

4.1.2. *Displacement evaluation*

Once particle images have been recorded, one has to find a way to accurately measure the displacement. The most efficient technique to adopt depends on the density of particles in the image.

As already mentioned, at high density the displacement can be measured from the speckle patterns (Laser Speckle Velocimetry, LSV). On the other end, at very low density the particles can be tracked individually, in this case we can talk about Particle Tracking Velocimetry (PTV). This simple approach

was very useful when computer capabilities were not adequate to perform more complex statistical operations. However, due to the low particle density, often the number of vectors per unit area is not large enough to fully resolve the flow field. However, as discussed in section 1.3.2, PTV is still a valuable tool for tracking bubbles and particles in many types of multiphase flows.

To increase the resolution, the particle density can still be raised to intermediate values between those typical of LSV and PTV. In this range it is impossible to univocally determine the displacement of the individual particles, so the strategy becomes to divide the images in many small interrogation areas and calculate the average displacement in each sub window. This can be done by thinking of each interrogation area as a 2-D signal of gray levels. Then, in a subsequent image, the same interrogation area will be a nearly identical but slightly shifted signal. Therefore, it is quite natural to think on cross correlating (or auto correlating in case of double exposed images) the two images. In this way, the maximum of the the cross correlation will correspond to the average shift between the two signals, which is nothing else than the average particle displacement in the 2-D plane defined by the area. In the case of a double exposure image, the auto correlation plane would be symmetric, and instead contain three main peaks, one for zero displacement and two peaks, symmetrically located around the center, due to the particle displacements (from which the directional ambiguity arises).

Due to the limited computer memory, in the 1980's this operation was performed optically, using the Optical Fourier Transform (OFT), which is the equivalent of the correlation in the frequency domain. The average displacement in that case was given by the orientation of the fringes generated in the OFT.

Nowadays instead, thanks to the increased computer speed and storage capacity, the interrogation is performed entirely digitally, and the displacement is calculated directly from the auto, or cross correlation plane.

4.1.3. *Accuracy and source of errors*

The accuracy of PIV first of all depends on the quality of the particle images.

Obviously, the quality of the images depends on the optical devices used to capture the images. For instance, phenomena like optical aberration can occur, and the result would be a distortion of the optical field. In that case, incorrect particle displacements would be measured. Therefore, this and similar phenomena should be minimized.

Furthermore, any kind of non-homogenity of the image plane, such as irregular seeding or gradients in the background illumination, results in a decrease of the Signal-to-Noise Ratio (SNR) in the correlation plane, where the SNR in PIV is defined as the difference between the maximum and the mean of the

correlation function divided by the standard deviation (mainly a measure of the noise level).

Digital imaging can help to partly compensate some of these problems (like non-uniform background illuminations). However there is a major issue introduced by the discrete nature of digital images that needs to be taken care of. In fact, digital images are formed by a finite number of pixels, thus the maximum of the correlation function is located in one of these discrete intervals. This in turn means that the measured displacement can only be a multiple of the physical pixel size. This problem is known as *peak locking*. To overcome this, several interpolation techniques have been proposed and sub-pixel accuracy can be achieved (see Raffel (1998)). The efficiency of these interpolation methods depends on the size of the seeding particles, which must be 2-3 times bigger than the pixel size (Westerweel 1997).

Furthermore, the fact that the interrogation windows are finite and not periodic introduces a systematic error. This is because, for increasing shifts less data are actually correlated. Thus for large displacements the correlation peak will be biased towards lower values (*bias error*). This can be compensated by weighting the correlation function with proper functions.

The accuracy of the measurements also depends on the the probability of detecting the correct peak in the correlation plane, which is connected to the number of possible particle pairs that enter the correlation calculation. This number is in general affected by three factors: the overall particle density N, the in plane displacement and the out of plane displacement. These three quantities can be summarized in one parameter called *effective particle image density*, defined as $N_I F_i F_o$, where N_I is the local particle density, F_i and F_o are factors expressing the percentage of particles leaving the measurement window in the in (F_i) and the out (F_o) of plane direction.

Flows with strong velocity gradients and strong 3D motion increase the in- and out-of-plane particle pair-losses, thus contributing to the total measurement error. Therefore it is important to adjust parameters like the time interval between the pictures and the size of the interrogation areas to reduce these effects to the minimum.

Keane & Adrian (1991) have shown that $N_I F_i F_o > 8$ is required to get 95% of valid detection for double exposure images, whereas single exposure, double frame PIV only requires $N_I F_i F_o > 5$. This means that five particles have to remain in the interrogation area from one picture to the other in order to get 95% probability of valid detection.

4.1.4. *State of the art PIV*

The evolution of the modern PIV systems was driven by the goal of studying turbulent flows. Turbulent flows involves high speed, high accelerations and a

wide range of scales. This requires high intensity illumination (small particles and short exposure times), and high resolution.

Hence the standard PIV package now consists of a high intensity pulsed laser, which are able to provide enough illumination for tracer particles of the range of few micron size in air and 10-30 micron in water, a high speed digital camera (or two, in the case of stereo-PIV) that can produce double frame, single exposure images and a software that perform interrogation by correlation.

To ensure good resolution and accurate measurements of flows with strong velocity gradients, the state of the art PIV codes are based on hierarchical algorithms that progressively reduce the size of the interrogation area by shifting and deforming the interrogation windows. For a comparison between different algorithms see Stanislas *et al.* (2005).

However, although initially designed for turbulence studies, PIV is a very powerful tool used for many type of flows, including, sometimes with the help of image processing, multiphase flows. Hence, the configuration of each particular system can vary from that described above, according to the characteristics of the flow to be studied.

4.2. Present processing algorithms

Tracer particles, light source and camera used in the present set up are those described in chapter 3. Particle images are captured on multiple frames with single exposure.

However, the captured images not only contain images of the tracer particles, but also some of the fibers that are still partly visible due to a non perfect IoR matching, dispersion and other impurities such as entrained air bubbles. If we want to apply PIV techniques to measure the velocity of the tracer particles, the presence of these other features would negatively affect the result of the displacement evaluation. For this reason, prior to the PIV algorithms, the images are processed with a custom made digital filter, which is described in the next section.

4.2.1. *Image processing*

To understand the meaning of *Image processing*, it is useful to think of an image as a function of two variables, $I(x, y)$, where I is an amplitude (*e.g.* brightness). On this basis *Image processing* can be defined as a series of operations that transform the input image $I(x, y)$ into an output image $I_o(x, y)$.

Instead, the process of performing measurements on an image (such as mean, standard deviation, *etc.*), is usually referred to as *Image analysis*.

In general, digital cameras store the elements of I as integer numbers. The number of intervals depends on the resolution of the analog to digital (AD) converter of the device used to acquire the image. If n is the number of bits of the converter, the number of intervals (often referred to as *bit depth*) is 2^n. In

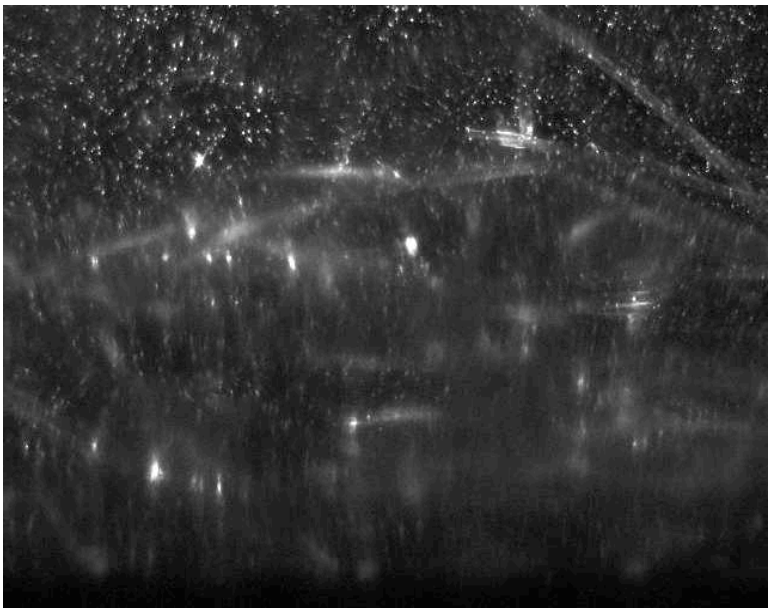

FIGURE 4.1. Typical image captured in the filtration experiment. The small bright spots are the seeding particles and the long structures are the fibers, visible due to the not perfect index of refraction matching.

digital imaging, also the continuous space defined by the coordinates (x, y) is discretized, and divided into N rows and M columns. The intersection between a row and a column is called *pixel*.

The advantage of working with digital images is that they can be stored in a computer memory, which makes it possible to use powerful mathematical tools such as convolution, Fourier transform and statistic analysis to process and/or analyze the image.

4.2.1a. *Feature detection.* Examples of image processing might vary from the simple operations of brightness or contrast adjustments, which can be accomplished with a single operation, to more complex tasks like extrapolation of contours or isolation of features, which instead require multistep algorithms and more advanced mathematical tools.

Our task belong to the latter category. Figure 4.1 shows a typical image captured in our experiments. In this image we have small bright spots with circular shape and more elongated, diffused structures on a dark background. The bright spots are the tracer particles, added to the suspension in order to visualize the motion of the fluid phase. The elongated structures are the fibers

that are still partly visible due to a non perfect IoR match and dispersion. The aim of the processing is to isolate the seeding particles and the fibers in two separate images.

In order to accomplish this, an algorithm able to distinguish between different features (for example between small round particles and large elongated structures) is needed. This is a well studied problem in image processing, which is commonly solved either by transforming the image into the curve parameters space (Hough transformation, see Duda & Hart (1972)) or by template matching. The latter consist of correlating the image to analyze with a template image that reproduces the shape of the objects one wants to detect.

Both techniques have been widely applied to the study of multiphase flows, to identify the different phases. Examples are Honkanen & Marjanen (2007) who used the Hough transformation to identify bubbles of irregular shape, Metzger *et al.* (2007) who applied the transformation to classify position and orientation of fibers during sedimentation. For the same purpose Carlsson *et al.* (2007) used a template matching technique, using a template function from the class of steerable filters (see Jacob & Unser (2004)). The latter approach was proven to be computationally very efficient.

From a mathematical point of view, the two methods are substantially equivalent, as demonstrated by Stockman & Agrawala (1977), and they work very well when the object to identify has well defined shape and contours. However, in our case the fibers are only partly visible, and the bits that are visible have irregular shapes and a diffuse color, which makes it impossible, or extremely inefficient to apply any of the techniques mentioned above to identify them.

On the other end, shape and color of the seeding particles are very well defined. However, due to the small size of the particles, applying a template matching (or Hough transform) technique is equivalent to apply a high-pass filter to the image, which generates high noise levels.

We therefore need to combine different tools to create a more complex filter able to discriminate between different particle sizes and shapes without introducing any additional noise.

4.2.1b. *Filter description.* The algorithm we adopted is similar to that described in Chung *et al.* (2007), where the authors want to isolate circular gas bubbles and eliminate out of focus particles. The algorithm, which is illustrated in figure 4.2 (as a flowchart) and in figure 4.3 (images), consists of the following steps:

(i) **Thresholding and Gamma adjustments.** The original image is divided in 64x64 sub-windows with 50% overlap and the local mean is subtracted from each sub-window (*Thresholding*). This compensates for

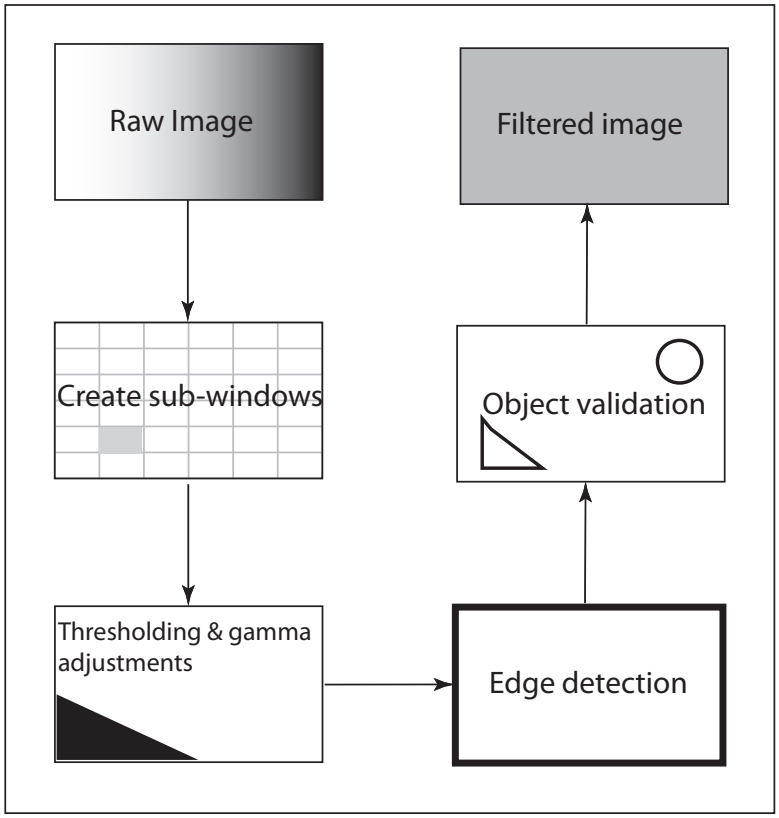

FIGURE 4.2. Flowchart of the image processing algorithm.

an uneven background illumination. Successively, an exponential operator is applied to maximize the contrast in each sub-window (*Gamma adjustment*, see figures 4.3(b) and 4.3(c)).

(ii) **Edge detection.** A binary image (black and white) containing the contours of each object of the image is created. (see figure 4.3(d))

(iii) **Object identification.** Area and perimeter of each particle is measured from the binary image created in step (ii). Consequently, the circularity of each object can be calculated as $c = d_A/d_p$, where d_A and d_p are the diameter calculated from the measure of the area and perimeter respectively. (figure 4.3(e))

(iv) **Validation.** The coordinates of particles with size and circularity in the desired range are recorded and the section of the original image corresponding to these particles pasted into a new image with a dark background. (see figure 4.3(f))

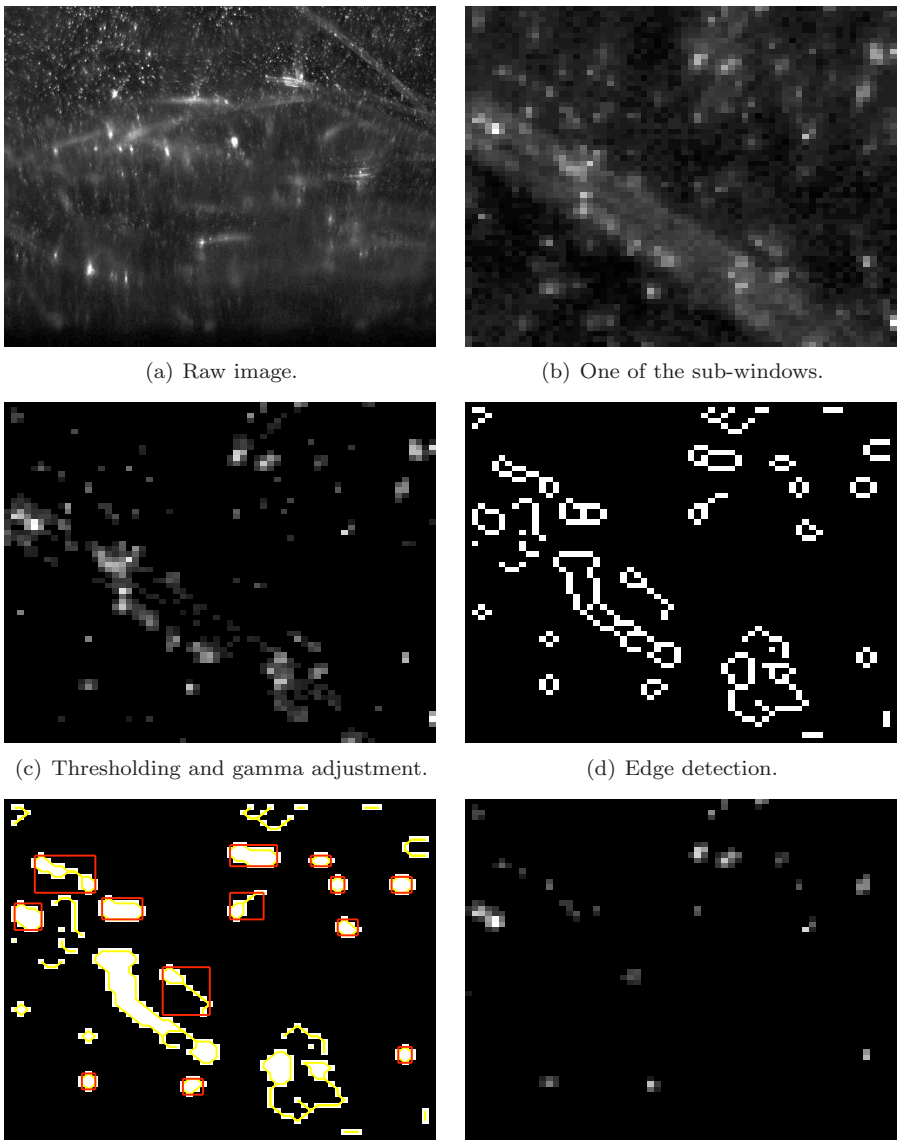

(a) Raw image.

(b) One of the sub-windows.

(c) Thresholding and gamma adjustment.

(d) Edge detection.

(e) Particle detection and selection.

(f) Filtered sub-image.

FIGURE 4.3. Image processing.

The algorithms were implemented using the image analysis toolbox of the commercial software ©MATLAB (version 2006b).

We have to point out that the need of digital image processing could be avoided if we used fluorescent seeding particles and an optical filter in front of the camera, see Towers *et al.* (1999). Here, the whit light source was preferred for simplicity. In addition to that, our algorithm provides statistical information of the particles, which can be used as a base for more advanced measurements.

4.2.2. *Displacement evaluation algorithm*

After the image processing described in section 4.2.1b and a Gaussian smoothing, we proceed to the displacement evaluation of the tracer particles. The latter is evaluated with an algorithm based on cross correlation techniques.

The interrogation algorithm is the following:

Step 1: Standard digital cross correlation with no window offset and 50% window overlap is performed. From the cross correlation plan, the location of the highest peak is detected and stored.
Step 2: The data is scanned to search for spurious vectors using predefined validation criteria based on SNR and Peak to Peak ratio. Spurious vectors are replaced with linear interpolation of valid neighbors.
Step 3: The displacement estimates are used to shift the second interrogation window locally by the nearest integer and reduce the window size.
Step 4: Repeat step 1 to 3 until the desired resolution is achieved.

The displacement is calculated with sub-pixel accuracy using a Gaussian fit. Bias error is also eliminated by weighting the correlation function prior to the peak detection.

4.3. Evaluation of the present algorithm

In this section, the present code is evaluated with a pair of artificial images, which simulate a known flow field. The simulated flow field is constructed so that vortices becomes smaller in size and stronger in vorticity from the top left to the bottom right.[1] In this flow field, the challenge for the code is to conciliate two contrasting requirements: small interrogation windows to resolve the small scales, and large in-plane displacements, which instead require large interrogation areas.

The multi-pass correlation with window shift adopted in our code allows us to start with a large interrogation window and use that estimate to apply the appropriate image shift in the next step, so that in-plane losses are minimized and the final resolution is obtained.

[1]The images have been developed by LaVison as a benchmark test for their commercial PIV softwares. LaVision is kindly acknowledged for providing us with these images.

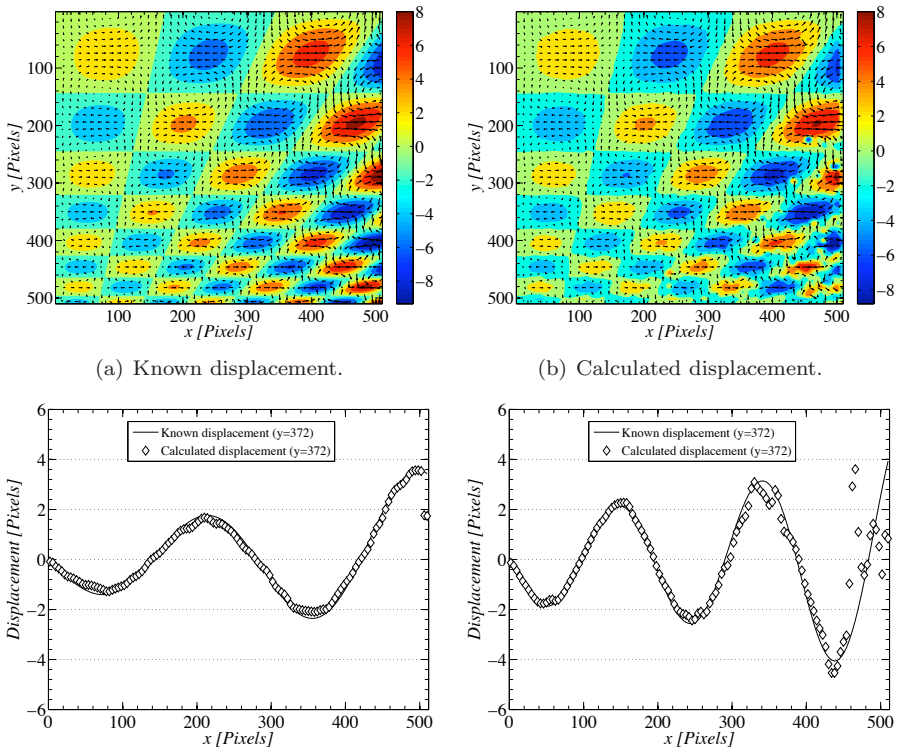

(a) Known displacement.

(b) Calculated displacement.

(c) y=160.

(d) y=372.

FIGURE 4.4. Contours of the known (a) and calculated (b) horizontal displacement in the test images. Plot (c) and (d) show the horizontal profile at y=160 (c) and y=372 (d) of the known (-) and calculated (◊) data.

However, our code does not adopt window deformation, therefore, we expect a large error in regions with strong gradients.

The known flow field and the one calculated with our code is shown in figure 4.4. The flow field has been calculated with an initial interrogation window of 64×64 pixels and a final window of 16×16 with 50% overlap. In order to compare the measurements with the known solution, the formers have been interpolated in a grid with 128×128 points.

In particular figure 4.4(a) and 4.4(b) show the contours of the known and measured horizontal displacement u, respectively. The displacement is expressed in pixels, which is also the unit of the x and y axes. Already from the contours we can see that the accuracy of the measurements deteriorates

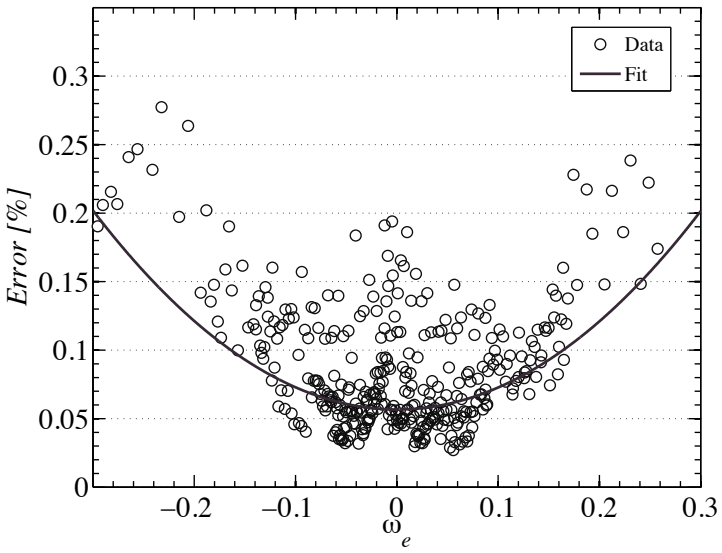

FIGURE 4.5. Relative error of the PIV measurements plotted vs. the flow vorticity (○). The curve (-) is a parabolic fit to the data.

going towards the bottom right part of the domain, due to the larger gradients. This is more evident in figure 4.4(c) and 4.4(d) where two measured profiles are compared to the known solution at y=160 and y=372. These plots show that the displacements are calculated with good accuracy where the gradients are moderate, but it is clear that the error increases in regions of strong gradients.

The correlations between measurement error and gradients in the flow is quantified in figure 4.5, where the error calculated from the data is plotted against the flow vorticity ω_e defined as:

$$\omega_e = \frac{1}{2}\left(\frac{\partial v_e}{\partial y} - \frac{\partial u_e}{\partial x}\right)$$

where u_e and v_e are the known horizontal and vertical displacements, respectively. The error is below 5% in regions where $-0.05 < \omega_e < 0.05$. However, the errors increases quadratically with the vorticity.

4.3.1. *Subpixel accuracy*

The accuracy of the subpixel inerpolation, and therefore of the overall accuracy, depends on the ratio between the size of the seeding particles (d_s) and the physical pixel size (d_p). In particular, a Gaussian interpolation works best for

a ratio $2 < d_s/d_p < 3$, whereas a lower ratio might cause peak-locking (see section 4.1.3).

For these reasons, the evaluation of subpixel accuracy has to be done in the actual experimental conditions, since the physical pixel size depends on the optical setup.

In our setup, the physical size pixel size is 28 μm. Thus $d_s/d_p < 1$, which might lead to peak locking. To avoid these, prior to the interrogation algorithm, we perform a gaussian smoothing on the images, which effectively increases the apparent size of the seeding particles.

In case of peak-locking the distribution of the measured displacement will be characterized by clear peaks around integer values, therefore an analysis of the displacement histograms is an effective way to detect this problem.

In figure 4.6 we show the histograms of three cases with different average displacements, where it is clear that the displacement distribution is smooth and not affected by peak locking.

4.3.2. *Particle losses due to image processing.*

An additional source of error is introduced by the image processing, since particle pairs can be lost due to the digital filtering. This can be caused by fibers obstructing the field of view in such a way that some tracer particles that are visible in the first image, cannot be detected in the next.

In low fiber density regions, this phenomena is negligible, but in regions of high fiber concentrations, like in the forming fiber network, this problem might cause major particle image losses. This sometimes reduces the particle image density, thus the probability of valid peak detection, to unacceptably low values. Therefore, in this work data in regions of high fiber concentration will be discarded.

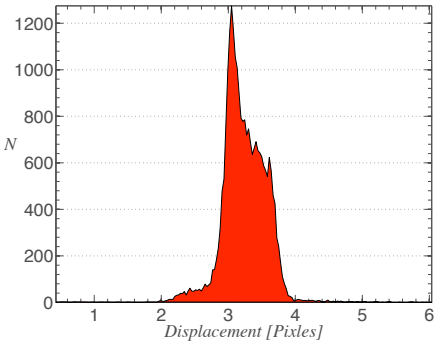

(a)

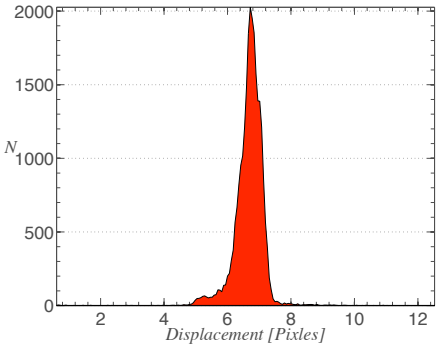

(b)

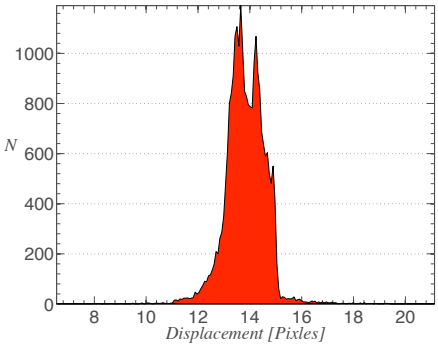

(c)

FIGURE 4.6. Histograms of PIV displacement data obtained from a sequence of 5 images of the flow from our experimental realizations. The histograms show that the measurements are not affected by peak-locking. The bin width is 0.1 pixels.

CHAPTER 5

Results

The data to be presented are divided into three main sections: validation of the apparatus, flow above the empty screen, and flow above the forming network during filtration. To facilitate the understanding of the data, we start with describing the statistical tools and the corresponding nomenclature we have adopted.

5.1. Nomenclature and statistical operators

The physical coordinates are X^*, Y^*, whose origin and direction is shown in figure 5.1: the axes originates at the intersection between the screen and the left wall, the X^* axis is positive from left to right and the Y^* axis is aligned with the direction of gravity. Here, they will be scaled in three different ways for (i) validation of the flow in the test section, (ii) investigations of the flow over the empty screen and (iii) studies of the flow over the forming network. The coordinates will be defined in the beginning of the respective sections. The physical velocity components (u^*, v^*) are always scaled with the drainage velocity, V_m:

$$u = \frac{u^*}{V_m} \qquad v = \frac{v^*}{V_m} \tag{5.1}$$

and time is scaled as

$$t = \frac{t^*}{t_s} \tag{5.2}$$

where t_s is the Stokes time, *i.e.* the time it takes for a single horizontal fiber to sediment one fibre diameter d_p.

The velocity field measured with PIV is time resolved, thus the velocity components u and v are functions of the two spatial coordinates x and y, and of the time t. Two statistical operators will be used: average and root-mean-square. They are denoted with an overbar (*e.g.* $\bar{u}$) and subscript *rms* (*e.g.* u_{rms}), respectively. Both operators will be applied in time as well as along the x-direction and the direction is denoted with subscript x or t. For example, $\bar{v}_x$ indicates the average of the vertical velocity component in the x-direction, whereas to indicate the *rms* in the same direction we will use the notation $v_{rms,x}$.

Equation (5.3) provides the explicit expressions of the operators that will be used most frequently:

$$\begin{aligned} \bar{v}_t(x,y) &= \tfrac{1}{N_t}\textstyle\sum_{k=1}^{N_t} v(x,y,t_k) \\ \bar{v}_x(y,t) &= \tfrac{1}{N_x}\textstyle\sum_{k=1}^{N_x} v(x_k,y,t) \\ v_{rms,x}(y,t) &= \sqrt{\tfrac{1}{N_x}\textstyle\sum_{k=1}^{N_x}(v(x_k,y,t)-\bar{v}_x)^2} \\ [\bar{v}_t]_{rms,x}(y) &= \sqrt{\tfrac{1}{N_t}\textstyle\sum_{k=1}^{N_x}(\bar{v}_t(x_k,y)-\bar{v}_{tx})^2} \end{aligned} \tag{5.3}$$

where N_x and N_t are the number of samples in the x direction and in time, respectively.

5.2. Characterization of the flow in the setup

In this section, the physical coordinates (X^*, Y^*) are scaled with the width of the test section $D = 80$ mm and the non-dimensional coordinates are:

$$X = \frac{X^*}{D} \qquad Y = \frac{Y^*}{D}. \tag{5.4}$$

5.2.1. *Experimental procedure*

In order to check the extension of the boundary layer in the test section and verify the assumptions made in section 3.1.1, we perform measurements of the flow in the near wall region. Each experiment (realization) consists of two parts. In the first part we fill the test section until the free surface level reaches $Y^* = -100$ mm. In the second part the flow is driven down until the surface is at $Y^* = -40$ mm. The position of the free surface is controlled with the loop in figure 3.2. The fluid used is water seeded with tracer particles. No fibers are suspended in the flow. Images of the flow are captured during the second part, where the fluid flows through the screen.

The measurement plane is illustrated in figure 5.1. The right edge of the image window is located at the left wall, and it has a physical width of 22.8 mm and height of 17.0 mm.

We performed three realizations at different flow rates. We will refer to the three realizations as **Case 1**, **Case 2** and **Case 3**. The test was done keeping the flow rate constant during the entire realization, except from a short, transient acceleration at the start up. The corresponding average drainage velocity (V_m) for each realization is shown in table 5.1. In the same table, the values of the Reynolds number Re_D based on the channel width $D = 80$ mm are also shown.

The velocity is measured with the PIV system described in section 4.2.2, and the settings of the PIV parameters are shown in table 5.2.

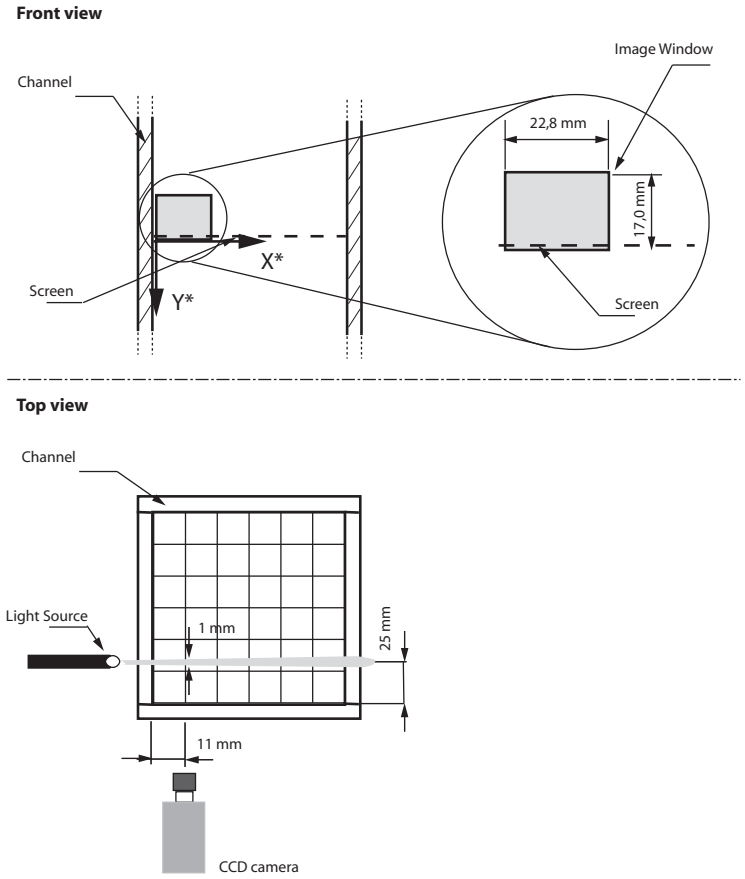

FIGURE 5.1. Schematic of the measurement area for **Case 1**, **Case 2** and **Case 3**. The positions of the light sheet and the camera with respect of the test section are defined in this figure. The position of the coordinate system (X^*,Y^*) is also shown. The close up illustrates the physical size of the image window (22.8×17.0 mm^2).

	Case 1	**Case 2**	**Case 3**
Average velocity [mm/s]	V_m=21.5	V_m=46.5	V_m=96.4
Reynolds number	Re_D =1565	Re_D =3378	Re_D=7011

TABLE 5.1. Setup verification: experimental cases.

PIV settings	$x-direction$	$y-direction$
# interrogation windows (N_x N_y)	79	59
Overlap [%]	50	50
Final interrogation window [Pixels]	16	16
Time between images [ms]	5	

TABLE 5.2. Setup verification: PIV settings.

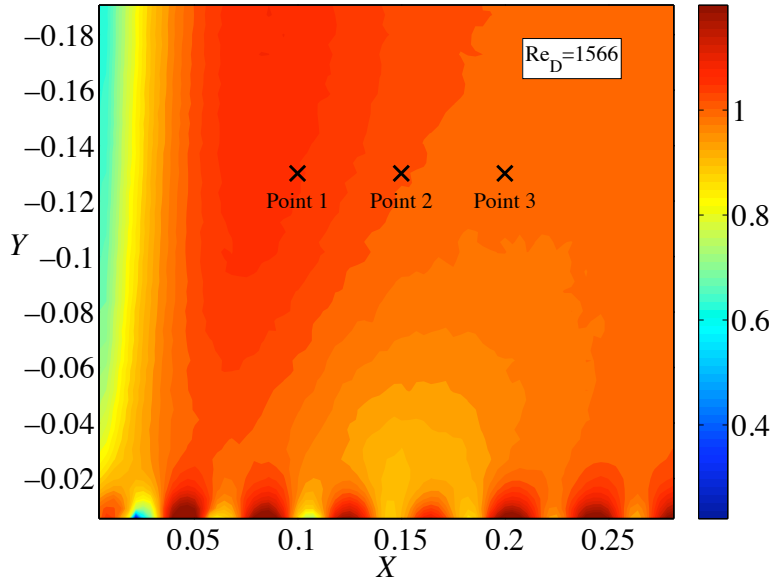

FIGURE 5.2. **Case 1**: Contours of the normalized mean velocity component $\bar{v}_t$. The average is computed from 57 instantaneous velocity field and over a time span of 3 s. The symbols ($\times$) show the location of Point 1, Point 2 and Point 3.

5.2.2. *Average flow field*

In figure 5.2 we show the time average of the normalized velocity component v for **Case 1**. Here we can see that in $0 < X < 0.025$, due to the presence of the wall, a region of low velocity has developed (the boundary layer). In $0.05 < X < 0.15$ instead, the velocity is higher than the average. However, for $X > 0.15$, the velocity can be considered fairly constant in the X-direction, at least until we do not get close to the screen ($Y > -0.1$).

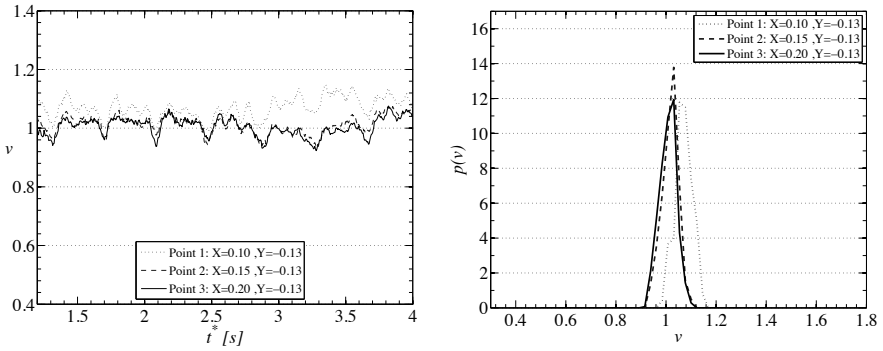

(a) Time series.

(b) Probability density functions.

FIGURE 5.3. **Case 1**: Time series (a) and probability density functions (b) of v for Point 1 ($\cdots$), Point 2 (- -) and Point 3 (–). The coordinates of the three points are $Y = -0.13$ and $X = 0.10$, $X = 0.15$ and $X = 0.20$, respectively. In (b), the bin width for v is 0.02.

5.2.3. *Time series and probability density functions*

Even if the average flow field can give an idea of the shape of the velocity profiles, the time series must be analyzed in several points to make sure that the velocity differences between different points are not too large at any time.

This is done in figure 5.3(a), where the time series of v are shown for three points. The three points are all located at $Y = -0.13$, but one of them is in the region $0.05 < X < 0.15$ (point 1), and the other two are in $X > 0.15$ (point 2 and point 3). The analysis of the times series confirm that in point 1, v is always higher than in point 2 and point 3, and that, most important, the time series in point 2 and point 3 are practically overlapping. From the time series we obtain the probability density functions of v in point 1, point 2 and point 3. These probability density functions are shown in figure 5.3(b), and they are consistent with the observations made in figure 5.3(a).

If we calculate the probability density function in the same way as in figure 5.3(b) for every point along $Y = -0.13$ and for every realization, we get (i) an idea of the shape of the velocity profiles in the channel, and (ii) the extension of the boundary layer as a function of Re_D. The contours of the probability density functions of $v(X, Y, t)$ for **Case 1**, **Case 2** and **Case 3** are shown in figure 5.4. It is clear that for every realization, there is a region where v is constant towards the center of the channel.

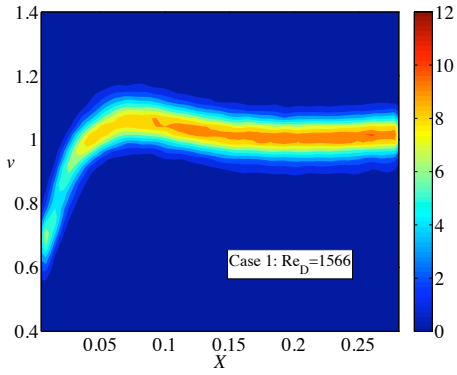

(a) Case 1.

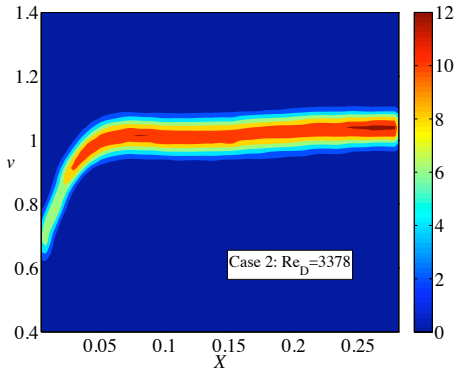

(b) Case 2.

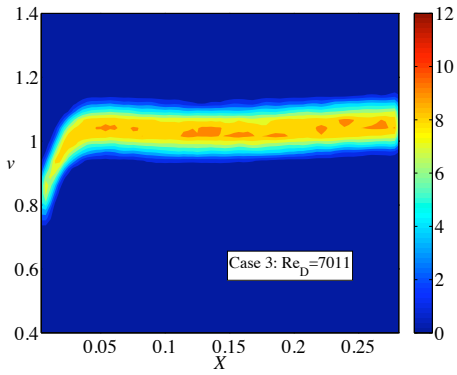

(c) Case 3.

FIGURE 5.4. Probability density functions of v for **Case 1** (a), **Case 2** (b) and **Case 3** (c).

PIV settings	$x-direction$	$y-direction$
# interrogation windows (N_x N_y)	24	53
Overlap [%]	50	50
Final interrogation window [Pixels]	16	16
Time between images [ms]	5	

TABLE 5.3. PIV parameters for the flow about the empty screen (section 5.3).

	Case 1	**Case 2**	**Case 3**
N_t	52	103	106
τ [s]	3	2.5	1

TABLE 5.4. Number of samples and time span for $\bar{v}_t$ and $\bar{u}_t$.

5.3. Flow above the empty screen

In this section we analyze in detail the flow above the screen in a region where $X > 0.2$, and therefore the velocity profiles are not affected by the side walls. The flow above the empty screen is important because it can be seen as the flow field generated by the filtration at $t = 0$, which determines the distribution of mass and orientation of the first layer of fibers in the network.

The results we present in this section are from the experimental conditions reported in table 5.1, whereas the new PIV settings are in table 5.3. The coordinates are scaled with the wire diameter of the screen $d_s = 1$ mm and the non-dimensional coordinates are:

$$x = \frac{X^* - X^*_C}{d_s} \qquad y = \frac{Y^*}{d_s} \tag{5.5}$$

where $X^*_C = 25$ mm is the center of the region under study.

5.3.1. *Average velocity field*

Figure 5.4 shows that the flow in the region $X > 0.2$ is stationary, thus it is sufficient to analyze the average velocity field. The latter is calculated from the time resolved measurements and the number of samples (N_t) and time span (τ) over which the averages are calculated are shown in table 5.4. Figure 5.5 shows the contours of $\bar{v}_t$ for **Case 1**.

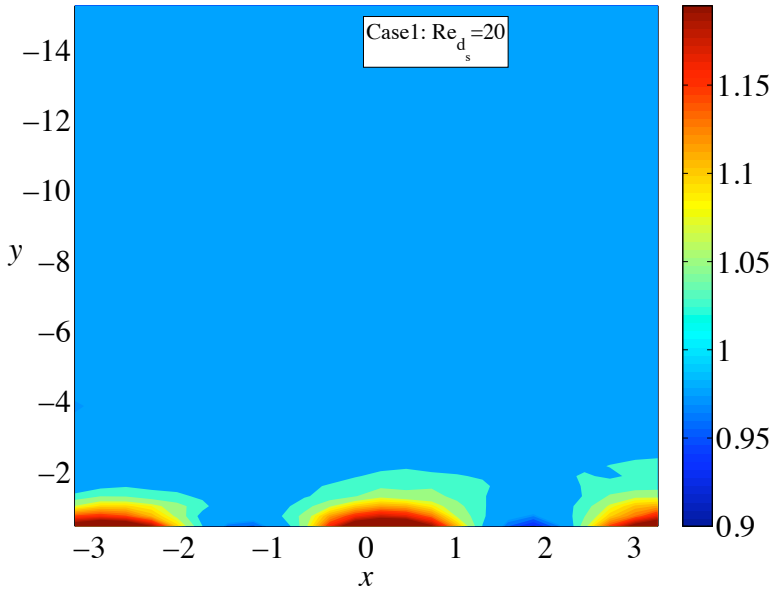

FIGURE 5.5. Mean vertical velocity $\bar{v}_t$ for **Case 1**. $\bar{v}_t$ is calculated from 52 instantaneous velocity measurements over a time span of 3 s.

5.3.2. *Velocity profiles and velocity fluctuations*

The mean velocity field $\bar{v}_t(x, y)$ for all the cases are shown in figure 5.6(a, c, e). In this figure we also show the normalized velocity profiles at four positions corresponding to y =-11.8, -8.1, 4.4, -0.7.

The velocity profiles start to deform as we get close to the screen but they appear quite unaffected by the screen further out. One way to quantify where and how much the velocity profiles start to deform is to analyze the *rms* of $\bar{v}_t$ in the horizontal direction, *i.e.* $[\bar{v}_t]_{rms,x}(y)$, which are shown in figure 5.6(b, d, f). The same analysis is repeated for the horizontal component u, and shown in figure 5.7. The variations in v are limited to $y > -2$ whereas for u, they start further out from the screen, around $y = -5$.

It is also interesting to compare the screen-normal profiles of $[\bar{v}_t]_{rms,x}$ and study the influence of Re_{d_s} on the level at which the fluctuations start to increase when approaching the screen. To do this, $[\bar{v}_t]_{rms,x}$ and $[\bar{u}_t]_{rms,x}$ are scaled with their respective maximum value and the results are shown in figure 5.8. It appears that the shape of the rms profiles is independent of the Re_{d_s}.

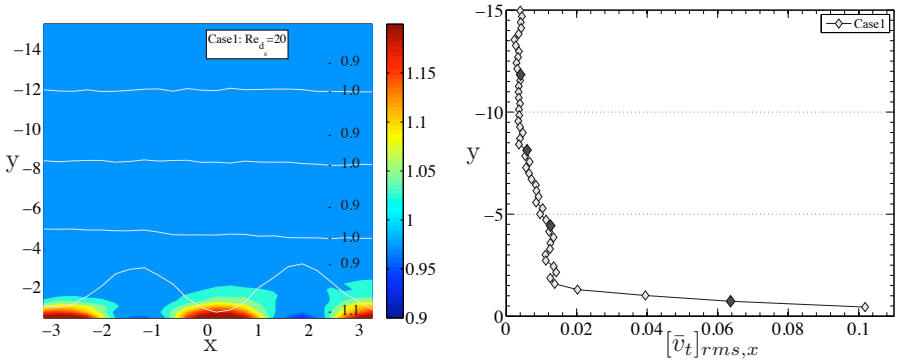

(a) Case 1, contours of $\bar{v}_t$.

(b) Case 1, $[\bar{v}_t]_{rms,x}$

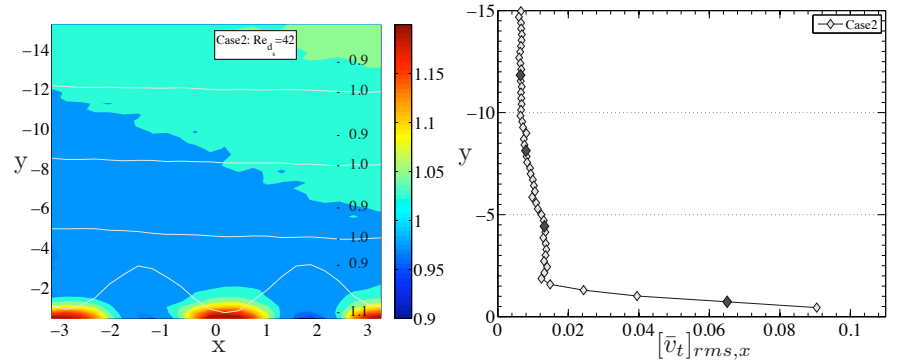

(c) Case 2, contours of $\bar{v}_t$.

(d) Case 2, $[\bar{v}_t]_{rms,x}$

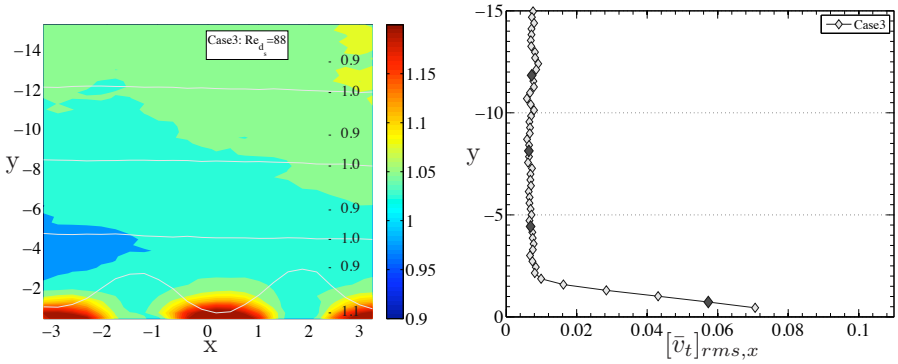

(e) Case 3, contours of $\bar{v}_t$.

(f) Case 3, $[\bar{v}_t]_{rms,x}$

FIGURE 5.6. Contours of $\bar{v}_t$ ((a, c, e) and screen normal profiles of $[\bar{v}_t]_{rms,x}$ (b, d, f) for **Case 1** (a, b), **Case 2** (c, d) and **Case 3** (d, f). The white lines in (a, c, e) show the normalized velocity profiles at y= -11.8, -8.1, -4.4 and -0.7.

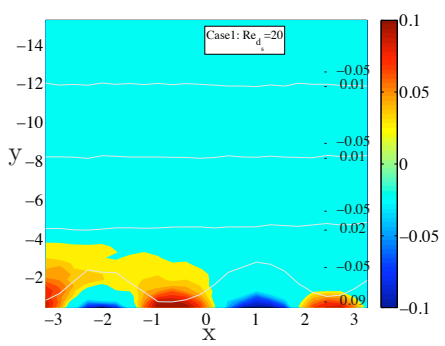

(a) Case 1, contours of $\bar{u}_t$.

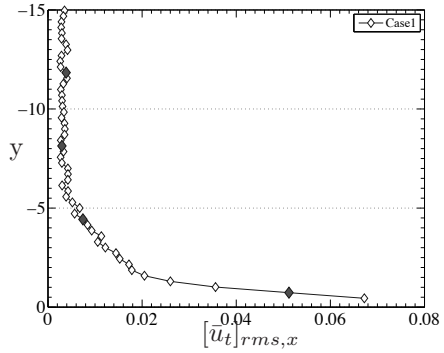

(b) Case 1, $[\bar{u}_t]_{rms,x}$

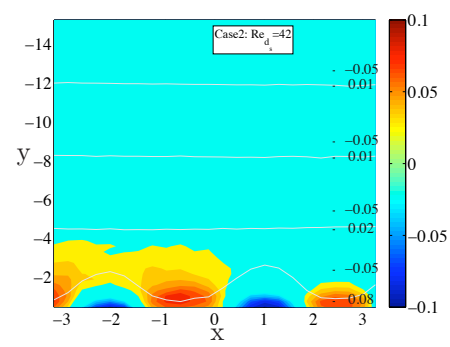

(c) Case 2, contours of $\bar{u}_t$.

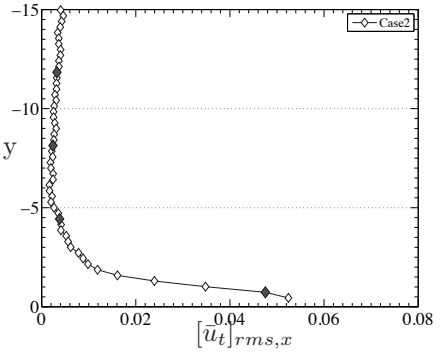

(d) Case 2, $[\bar{u}_t]_{rms,x}$

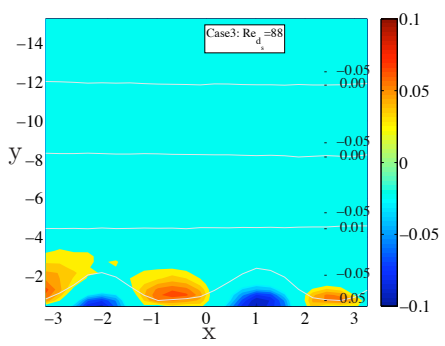

(e) Case 3, contours of $\bar{u}_t$.

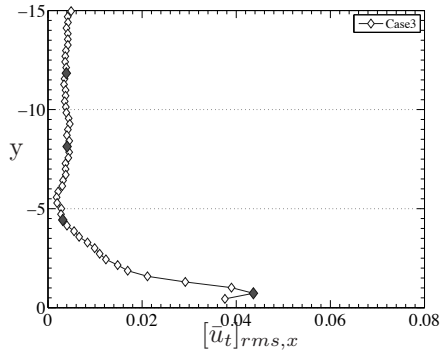

(f) Case 3, $[\bar{u}_t]_{rms,x}$

FIGURE 5.7. Contours of $\bar{u}_t$ (a, c , d) and screen normal profiles of $[\bar{u}_t]_{rms,x}$ (b, d , f) for **Case 1** (a, b), **Case 2** (c, d) and **Case 3** (d, f). The white lines in (a, c, e) show of the normalized velocity profiles at y= -11.8, -8.1, -4.4 and -0.7.

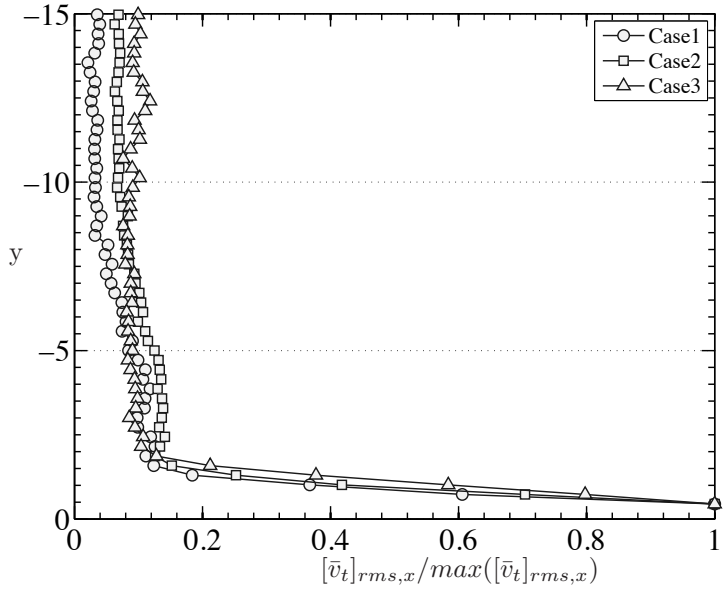

(a)

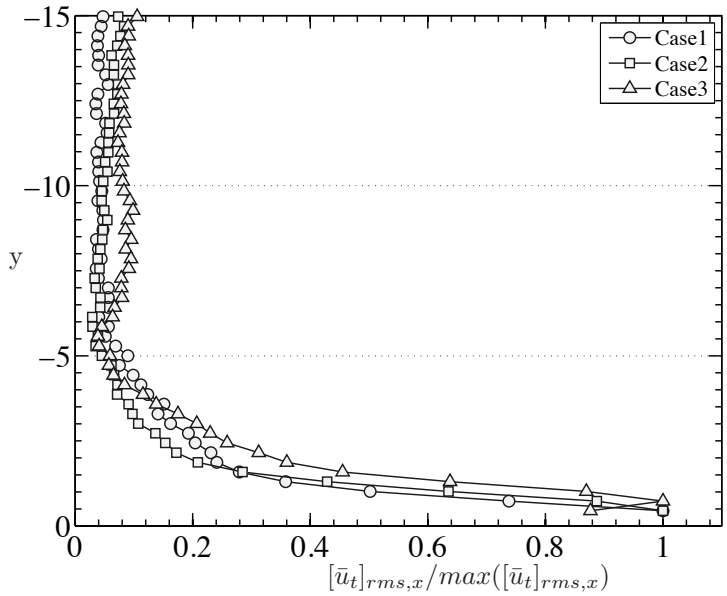

(b)

FIGURE 5.8. Normalized screen-normal profiles of (a) $[\bar{v}_t]_{rms,x}$ and (b) $[\bar{u}_t]_{rms,x}$ for **Case 1**, **Case 2** and **Case 3**.

5.3.3. *Velocity gradients*

As mentioned in chapter 2, the strain rate and vorticity determines the rotation rate of the fibers, and thus the orientation distribution. The shearing strain rate ϵ and vorticity ω in the 2-D plane of the measurements are defined as

$$\omega = \frac{1}{2}\left(\frac{\partial v}{\partial x} - \frac{\partial u}{\partial y}\right) \quad \epsilon = \frac{1}{2}\left(\frac{\partial u}{\partial y} + \frac{\partial v}{\partial x}\right) \tag{5.6}$$

and can be calculated from the 2D PIV-data. The results are shown in figure 5.9 for the vorticity, and figure 5.10 for the strain rate.

Figure 5.9(a, c, e) shows the contours of ω. It is clear that the vorticity is close to zero in a large part of the domain, and increases only in a thin region near the screen. This is further illustrated by figure 5.9(b, d, f), which shows $\bar{\omega}_x$ as a function of y. The maximum value of (the non-dimensional) $\bar{\omega}_x$ is decreasing with increasing Re_{d_s}, although the height over the screen at which they start to increase is fairly constant, in the range of Reynolds number we have investigated. Figure 5.10 shows the same type of plots for the strain rate ϵ, where a similar behavior as that of the vorticity can be observed. Note, however, that the strain extends slightly further out from the screen, as compared to the vorticity.

The normalized screen-normal profiles of $\bar{\omega}_x$ and $\bar{\epsilon}_x$ are compared in figure 5.11(a) and (b), respectively. The profiles show a strong similarity in the parameter range under study.

5.3.4. *Boundary region*

Figures 5.8 and 5.11 show that the flow perturbations are confined in a thin region near the screen.

This result is of interest because in regions where the velocity field is uniform, no relative motions between the fibers is possible. In fact, changes in the distribution of mass and orientation of the fibers due to hydrodynamic effects are only possible in regions where the velocity gradients are non zero. Although this analysis does not expose how the suspension microstructure is modified, it provides an estimation of the length scale over which the boundary can interact with the suspension. Here the height of the boundary region y_b can be defined as the level at which the 85% of the total "energy" ($E_{(f)}$) of a given quantity f is confined. Thus $y_{b(f)}$ is defined so that:

$$\frac{\int_0^{-y_{b(f)}} f(y)^2 dy}{E_{(f)}} = 0.85 \tag{5.7}$$

$$E_{(f)} = \int_0^{-y_{max}} f(y)^2 dy \tag{5.8}$$

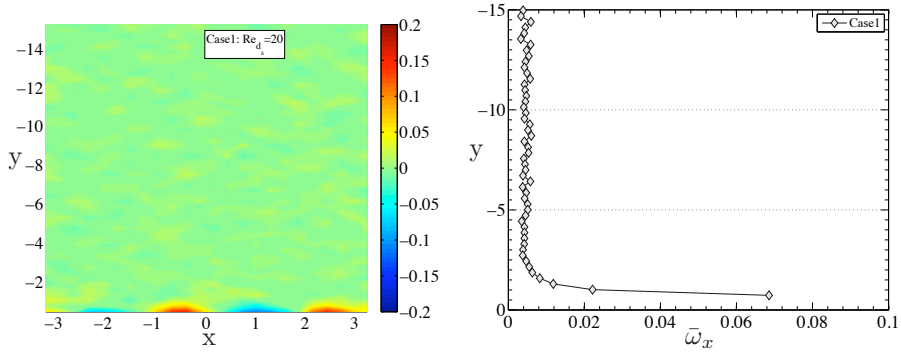

(a) Case 1, contours of ω. (b) Case 1, $\bar{\omega}_x$

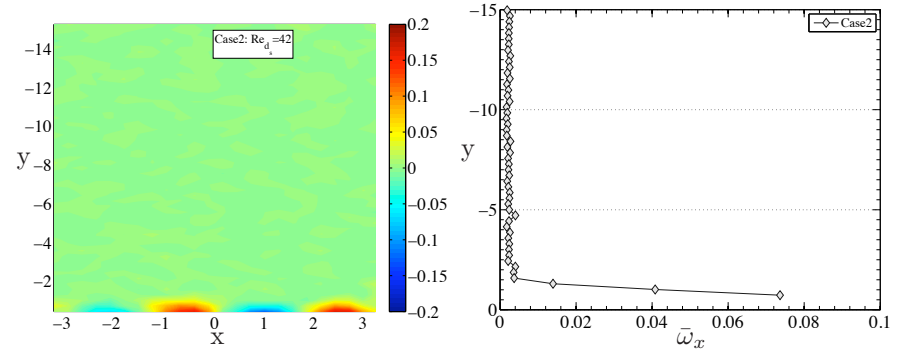

(c) Case 2, contours of ω. (d) Case 2, $\bar{\omega}_x$

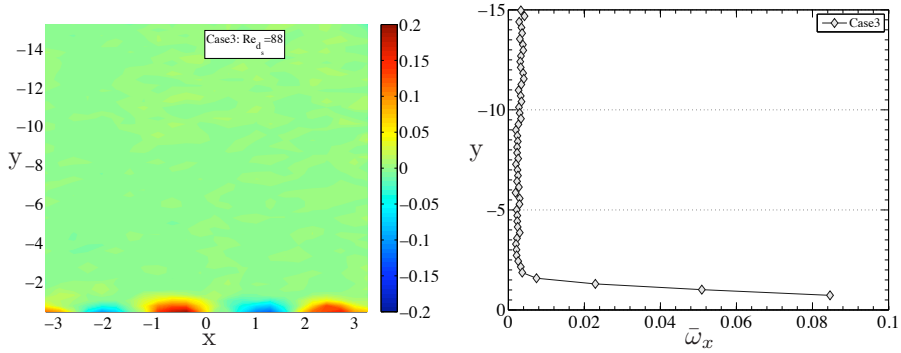

(e) Case 3, contours of ω. (f) Case 3, $\bar{\omega}_x$

FIGURE 5.9. Contours of ω (a, c, e) and the profiles of $\bar{\omega}_x$ as a function of y (b, d, f) for **Case 1** (a, b), **Case 2** (c, d) and **Case 3** (e, f).

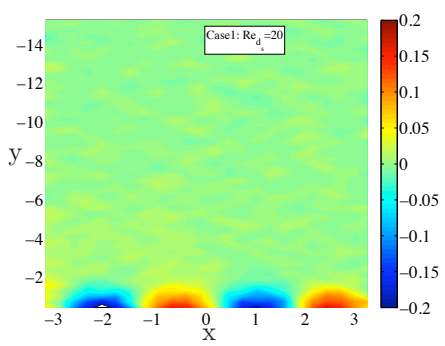

(a) Case 1, contours of ϵ.

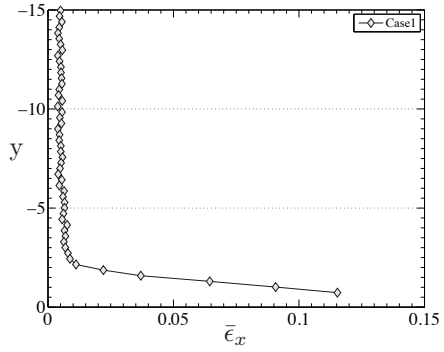

(b) Case 1, $\bar{\epsilon}_x$

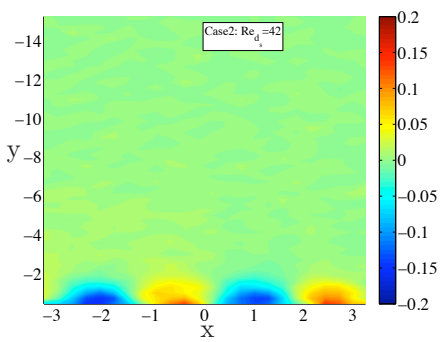

(c) Case 2, contours of ϵ.

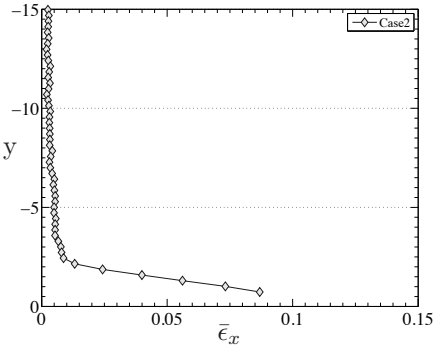

(d) Case 2, $\bar{\epsilon}_x$

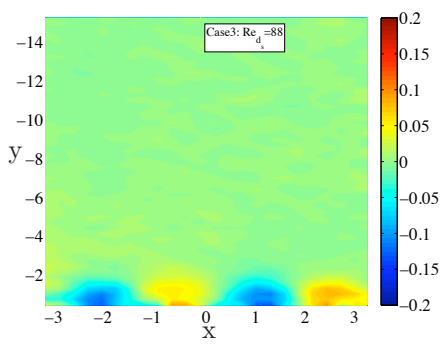

(e) Case 3, contours of ϵ.

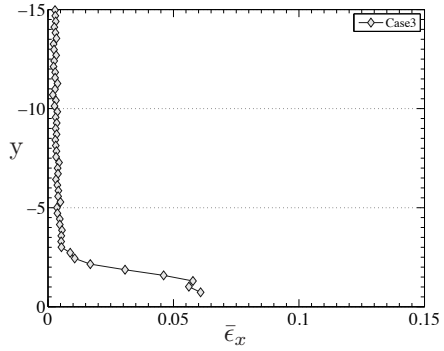

(f) Case 3, $\bar{\epsilon}_x$

FIGURE 5.10. Contours of ϵ (a, c, e) and the profiles of $\bar{\epsilon}_x$ as a function of y (b, d, f) for **Case 1** (a, b), **Case 2** (c, d) and **Case 3** (e, f).

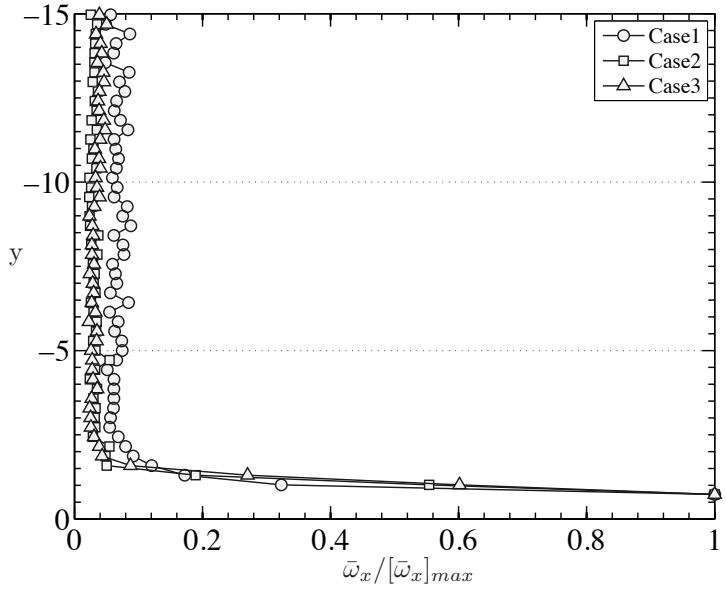

(a)

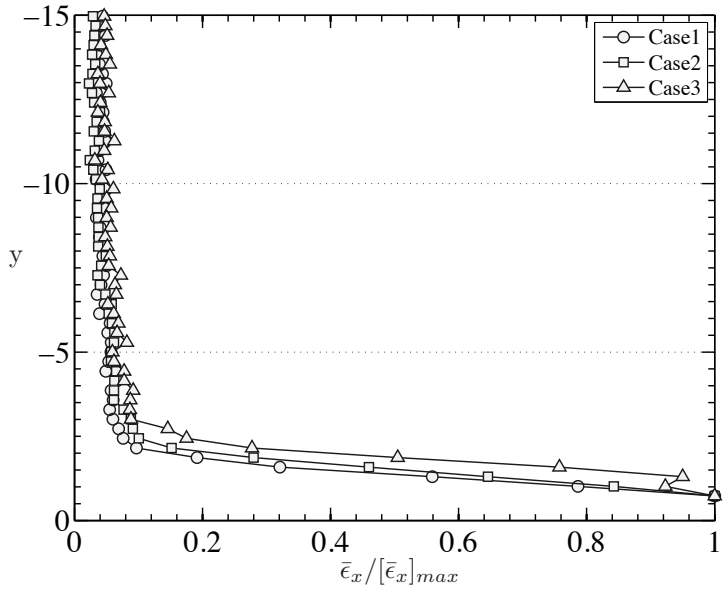

(b)

FIGURE 5.11. Normalized screen-normal profile of $\bar{\omega}_x$ (a) and $\bar{\epsilon}_x$ (b).

	Case 1	**Case 2**	**Case 3**
$y_{b([\bar{v}_t]_{rms,x})}$	-1.87	-3.72	-4.50
$y_{b([\bar{v}_t]_{rms,x})}$	-1.87	-1.30	-2.15
$y_{b(\bar{\omega}_x)}$	-3.86	-0.73	-0.73
$y_{b(\bar{\epsilon}_x)}$	-1.16	-1.16	-1.44

TABLE 5.5. Summary of y_b measurements.

where y_{max} is the total height of the image. From figures 5.8 and 5.11 we see that $-5 < y_b < -1$ for all quantities in the flow above the empty screen. The numerical values of the measured y_b are summarised in table 5.5.

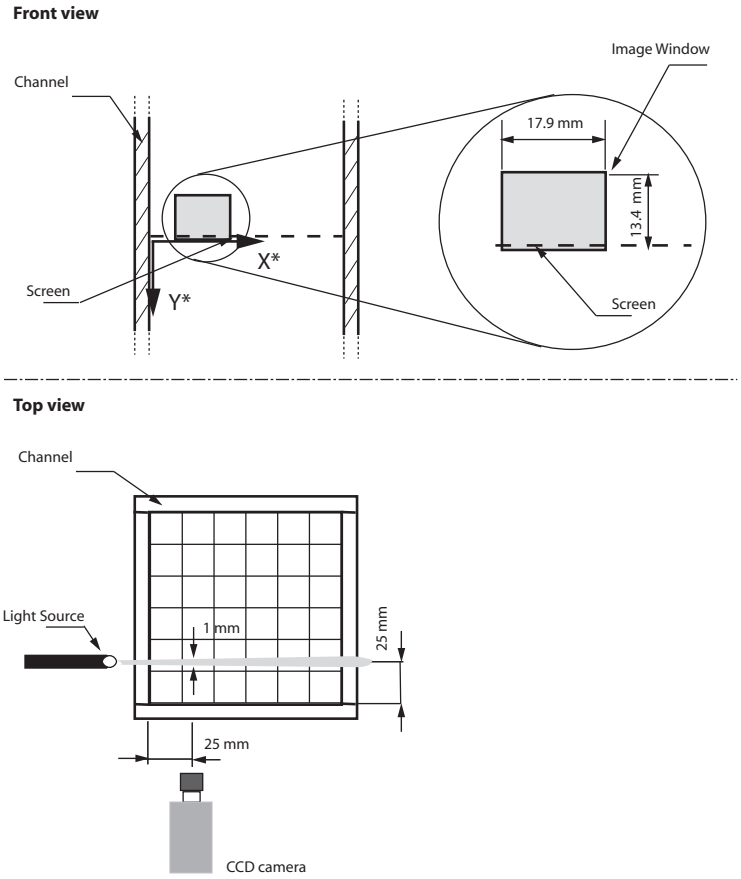

FIGURE 5.12. Position of the image window with respect to the coordinate system (X^*,Y^*) for the measurements presented in section 5.4. The camera is centered at $X_C^* = 25$ mm. In the close up the physical size of the image window (17.9×13.9 mm^2) is shown.

5.4. Flow above the forming network

In this section we present measurements of the velocity field generated by the filtration of a fiber suspension in the direct proximity of the forming fiber network. The coordinates are here scaled with the fiber diameter $d_p = 0.26$ mm so that

$$x = \frac{X^* - X_C^*}{d_p} \qquad y = \frac{Y^*}{d_p} \tag{5.9}$$

where X_C^* is the center of the region under study, in this case $X_C^* = 25$ mm.

5.4.1. *Experimental procedure*

The initial volume concentration of the suspension is about $\phi = 0.005$ for all the experiments. The concentration measure $N = \phi r^2$ is N=26 for the suspension with the long fibers and N=6.5 for the suspension with the short fibers. In both cases N is in the semi-dilute range (see section 1.2.2).

Each realization consists of filling the test section until the suspension reaches $Y^* = -150$ mm, gently stirring the suspension with a propeller until a homogeneous distribution is obtained. The end of the stirring coincides with the beginning of the filtration phase, where the suspension is filtered through the screen until the free surface has reached $Y^* = -40$ mm. The suspension is seeded with tracer particles and images of the flow are captured during the filtration phase.

The position of the measurement plane is shown in figure 5.12. The center of the image window is located at $X = 0.35$. The fluid, the fibers, the camera and the tracer particles used for these experiments are those described in chapter 3, and their properties are summarized in table 3.2.

The results in this section originate from six different cases, with all combinations of 3 different filtration velocities V_m, constant during each realization, and 2 fiber aspect ratios r. For each case we performed three realizations. At first sight, three realizations are far from enough to get converged statistics. However, thanks to the large amount of data generated by each realization, it will be seen that solid conclusions can be made. The cases are denoted **Case A**, **Case B**, **Case C**, **Case D**, **Case E** and **Case F**, whereas the three realizations will be denoted by the progressive numbers 1, 2 and 3.

The values of fiber length l_p, filtration velocity V_m, Stokes velocity v_s (as defined in eq. 2.16) and Stokes time $t_s = d_p/v_s$, for each case are presented in table 5.6. Table 5.7 contains the values of the non-dimensional parameters r, Re_{d_s}, Re_{d_p} and Se. The flow field is calculated with the PIV techniques described in section 4.2.2, and the settings of the PIV parameters are shown in table 5.8.

5.4.2. *Instantaneous velocity field*

Four snapshots of the instantaneous velocity v for **Case A1** at different times are shown in figure 5.13. The average level h_f of the fiber network is shown by the dark area in the figures. The figure shows that the flow structures are not stationary, hence the flow quantities has to be analyzed as a function of time. In (a), there is an acceleration in a narrow region close to the screen as observed before. As the network grows, larger flow structures appear in (b), (c) and (d).

Filtration velocity [mm/s]:		
$V_m = 20.5$	**Case A**	**Case B**
$V_m = 55.0$	**Case C**	**Case D**
$V_m = 75.2$	**Case E**	**Case F**
Fiber length [mm]:	l_p=18.8	l_p=9.4
Stokes velocity [mm/s]:	v_s =1.4	v_s =1.2
Stokes time $t_s = \frac{d_p}{v_s}$ [s]:	t_s=0.19	t_s=0.22

TABLE 5.6. Physical parameters of the experimental cases in section 5.4.

	Case A	**Case C**	**Case E**
$r = \frac{l_p}{d_p}$	r=72	r=72	r=72
$Re_{d_m} = \frac{\rho_f V_m d_m}{\mu}$	Re_{d_m}=1.64	Re_{d_m}=4.4	Re_{d_m}=6
$Re_{d_p} = \frac{\rho_f V_m d_p}{\mu}$	Re_{d_p}=0.43	Re_{d_p}=1.14	Re_{d_p}=1.56
$Se = \frac{v_s}{V_m}$	Se=0.068	Se=0.026	Se=0.019

	Case B	**Case D**	**Case F**
$r = \frac{l_p}{d_p}$	r=36	r=36	r=36
$Re_{d_m} = \frac{\rho_f V_m d_m}{\mu}$	Re_{d_m}=1.64	Re_{d_m}=4.4	Re_{d_m}=6
$Re_{d_p} = \frac{\rho_f V_m d_p}{\mu}$	Re_{d_p}=0.43	Re_{d_p}=1.14	Re_{d_p}=1.56
$Se = \frac{v_s}{V_m}$	Se=0.059	Se=0.022	Se=0.016

TABLE 5.7. Non-dimensional parameters.

5.4.3. *Fiber accumulation*

In this section the time evolution of the average fiber network level h_f is shown. The measure is extracted from the raw images analyzing the average grayscale values. This method exploit the fact that the regions with high fiber density

PIV settings	$x-direction$	$y-direction$
# interrogation windows (N_x N_y)	39	29
Overlap [%]	50	50
Final interrogation window [Pixels]	32	32
Time between images [ms]	5	

TABLE 5.8. Flow during filtration: PIV settings.

have an average brightness higher than regions with only seeding particles. The resulting network level for all realizations are shown in figure 5.14. Observe that the final network height is similar for all cases even though the temporal development of the height varies slightly. The only exception is **Case F**, where the final network level is considerably lower for the third realization. This is probably due to the fact that a portion of the fibers have been lost through the screen due to the combination of high filtration speed and short fibers.

Another observation that can be done is that for **Case B**, **Case D** and **Case F** the network level at $t = 0$ is not zero, this is because of a slight time shift from the start of the filtration and the capturing of the first image.

5.4.4. *Temporal development of the velocities*

The time evolution of the average vertical and horizontal velocity $\bar{u}_x$ and $\bar{v}_x$ are shown in figures 5.15 and reffig:TSu, respectively. The plots show that for the cases with the lowest filtration speed, **Case A** and **Case B**, there are large fluctuations around V_m for $\bar{v_x}$ and around zero for $\bar{u_x}$. The amplitude of the fluctuations is smaller for **Case C**, **Case D**, **Case E** and **Case F**.

The magnitude of the fluctuations over one realization can be quantified by the root-mean-square in time of the spatially averaged velocities. Figure 5.17 shows $[\bar{u}_x]_{rms,t}$, and the results are plotted as a function of Se, the natural sedimentation speed of the fiber divided with the imposed filtration speed. Each point in the figure is the average of the three realizations. The figure confirms that the level of fluctuations increases with increasing Se (decreasing V_m). Furthermore, the fluctuation amplitude is larger for short fibers than for long fibers.

5.4.5. *Velocity fluctuations*

In order to quantify the deformation of the velocity profiles, in section 5.3.2 we investigated the horizontal rms of the average velocity field. In a similar fashion, but for the instantaneous velocity field, here we calculate $v_{rms,x}$ and $u_{rms,x}$.

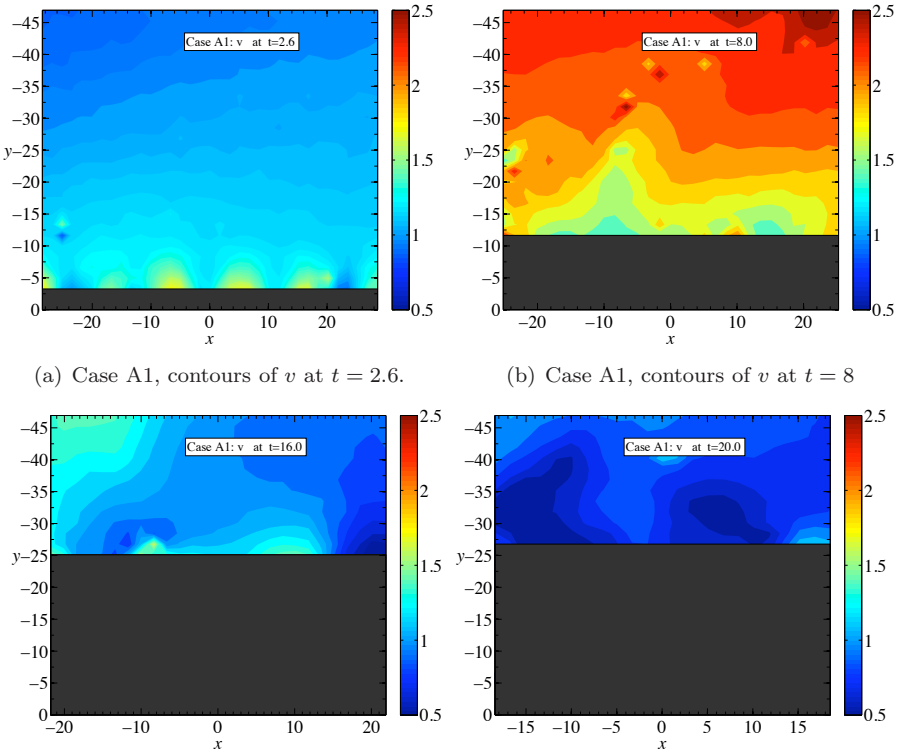

(a) Case A1, contours of v at $t = 2.6$.

(b) Case A1, contours of v at $t = 8$

(c) Case A1, contours of v at $t = 16$

(d) Case A1, contours of v at $t = 20$

FIGURE 5.13. Contours of v for **Case A1**, at $t = 2.6, 8.0, 16.0$ and 20.0. The dark area is the average level of the fiber network, calculated from the analysis of the digital images.

However, while in section 5.3.2 $[\bar{v}_t]_{rms,x}$ and $[\bar{u}_t]_{rms,x}$ were functions of y, in this case, $v_{rms,x}$ and $u_{rms,x}$ are functions of time as well.

First, $v_{rms,x}$ and $u_{rms,x}$ are calculated for the three realizations of each case. The final $v_{rms,x}$ and $u_{rms,x}$ for one case is obtained as the average over the three realizations.

The statistic consistency of this operation can be proved by looking at figures 5.14, 5.15 and 5.16. Here we see that the three realizations from each case are consistent with each other, showing similar behaviors, both in terms of formation of the fiber network and of average velocities. Hence, for the same case, we can expect similar flow statistics.

Figures 5.18 and 5.19 show the contours of $v_{rms,x}$ and $u_{rms,x}$ in the (y, t) plane, for all the cases. The average profile of the forming network is shown by

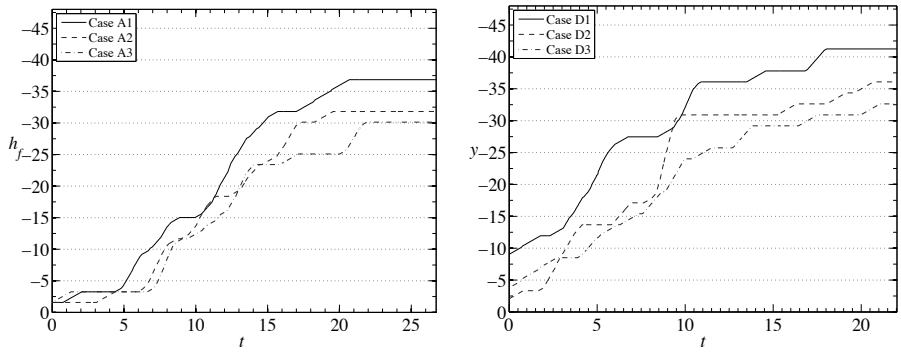

(a) Case A

(b) Case B

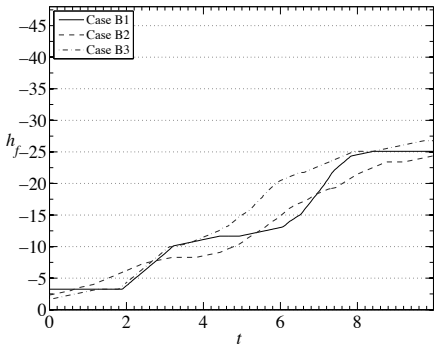

(c) Case C

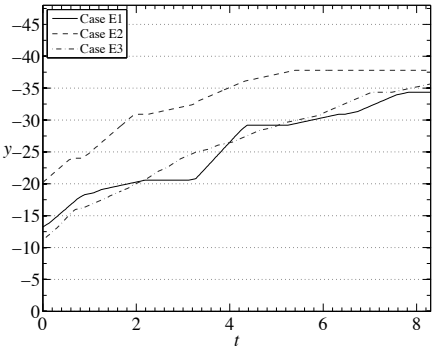

(d) Case D

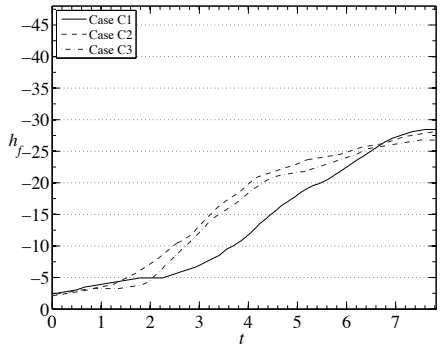

(e) Case E

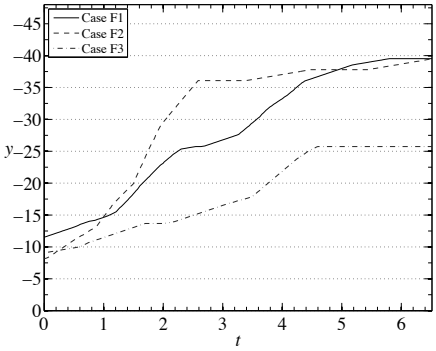

(f) Case F

FIGURE 5.14. Evolution of the average height h_f of the fiber network, calculated from the analysis of the grayscale of the images.

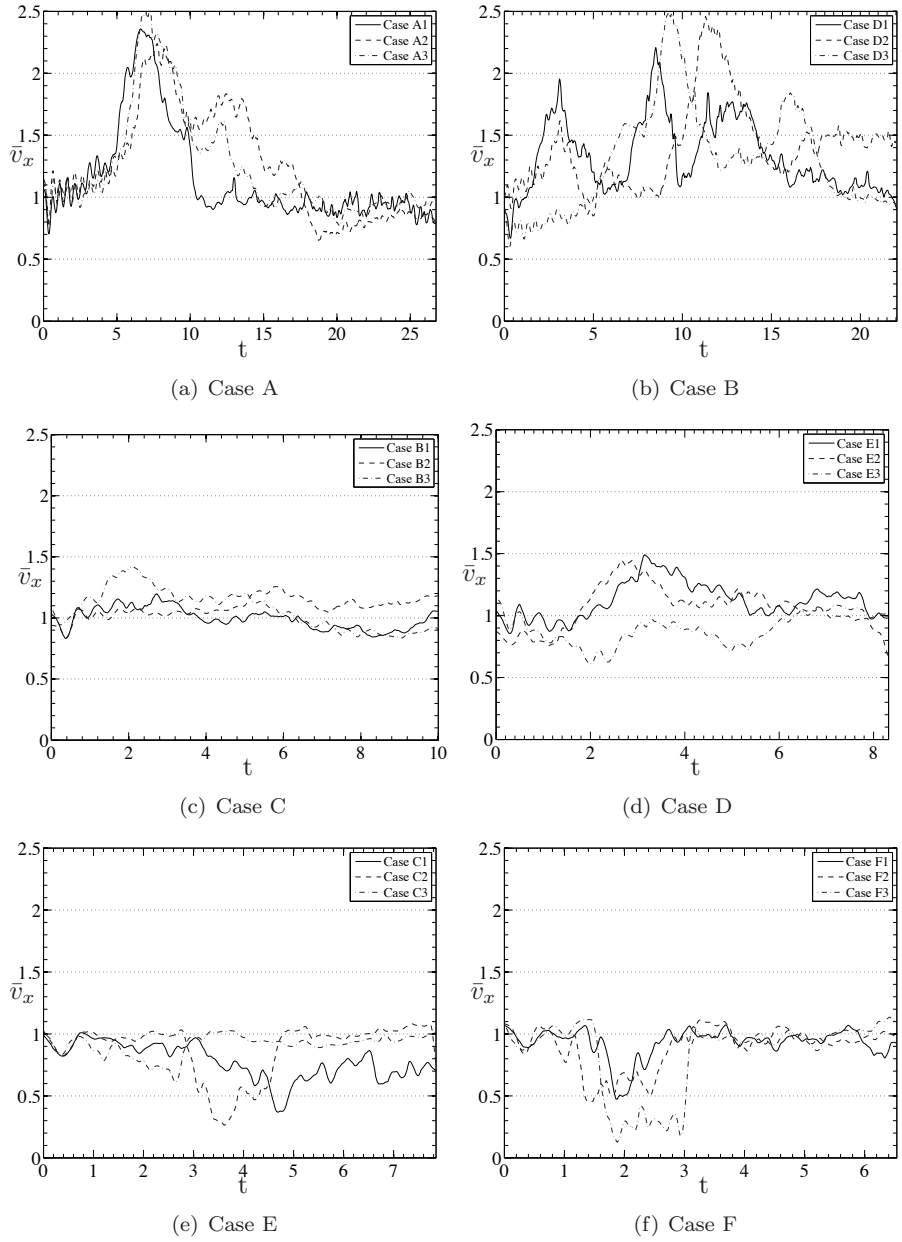

(a) Case A (b) Case B

(c) Case C (d) Case D

(e) Case E (f) Case F

FIGURE 5.15. Time evolution of $\bar{v}_x$ at y= -39 for the three realizations of all cases.

the darker region. From these plots we can see that regions of high activity in the proximity of the network can be observed for the fast long fibre cases, **Case C** and **Case E**, whereas the correlation is less distinct for **Case A**, **Case B**, **Case D** and **Case F**.

5.4.6. *Boundary region*

As in section 5.3.4, the height of a boundary region can be defined as

$$\frac{\int_0^{-y_{b(f)}(t)} f(y,t)^2 dy}{E_{(f)}(t)} = 0.85 \tag{5.10}$$

$$E_{(f)}(t) = \int_0^{-y_{max}} f(y,t)^2 dy. \tag{5.11}$$

As it appears from the equations, y_b and E are a function of time. Moreover, since the height of the boundary is also changing in time, the relevant measure becomes $y_b - h_f$.

The thickness of the boundary region has been calculated with $f = v_{rms,x}$ and $f = u_{rms,x}$; the results are shown in figures 5.20. The results show that $y_b - h_f$ is time dependent. In most of the cases, at $t = 0$ we have $-20 < (y_b - h_f) < -15$. However, the general trend is that $y_b - h_f$ first increases with time as the network is formed, reaches a maximum, and then saturates at a fairly steady value. The final value is $(y_b - h_f) \approx 10$ for the cases with long fibers, but it is slightly lower for the cases with short fibers.

The same trend is observed for E_f (figure 5.21), where the energy of the fluctuations reaches a maximum and then goes back to the initial value for the cases with short fibers, and to a value slightly higher for the cases with long fibers.

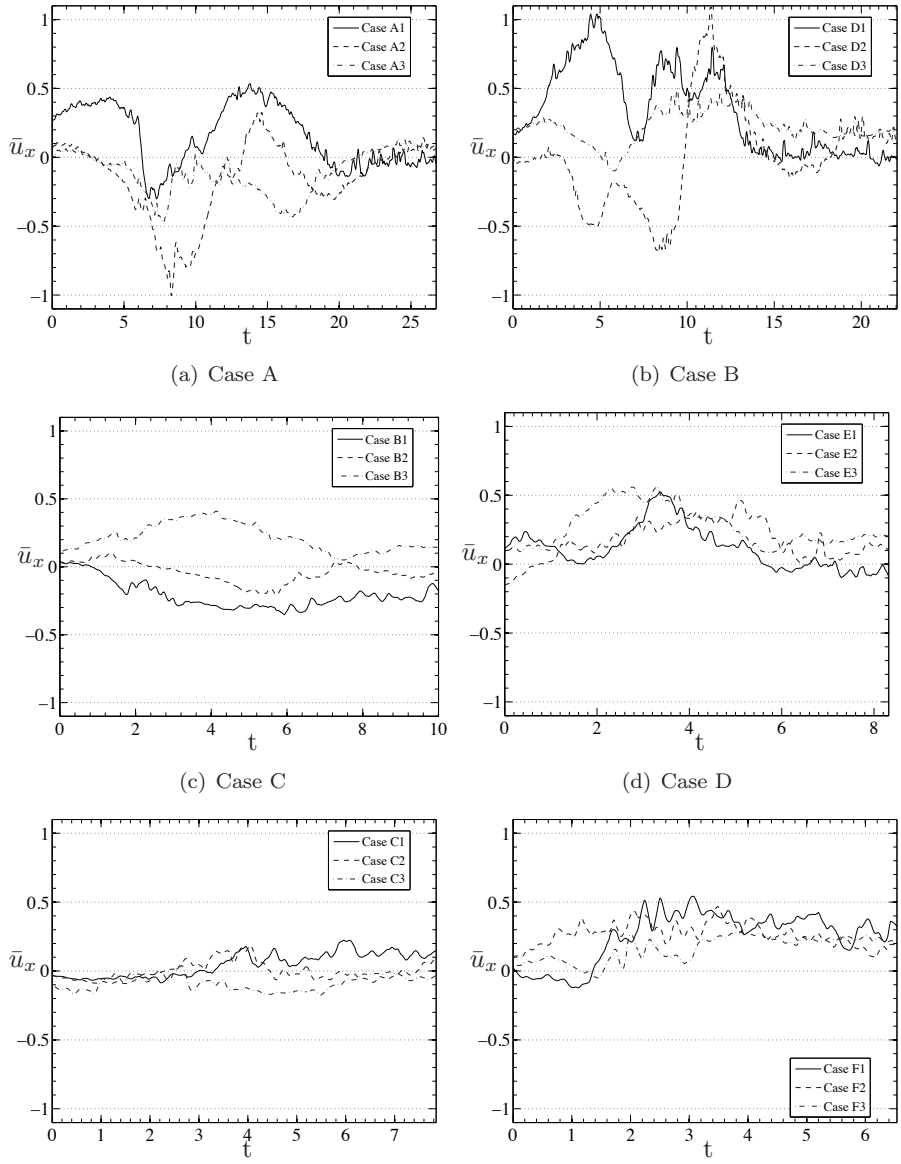

(a) Case A (b) Case B

(c) Case C (d) Case D

(e) Case E (f) Case F

FIGURE 5.16. Time evolution of $\bar{u}_x$ at y= -39 for the three realizations of all cases.

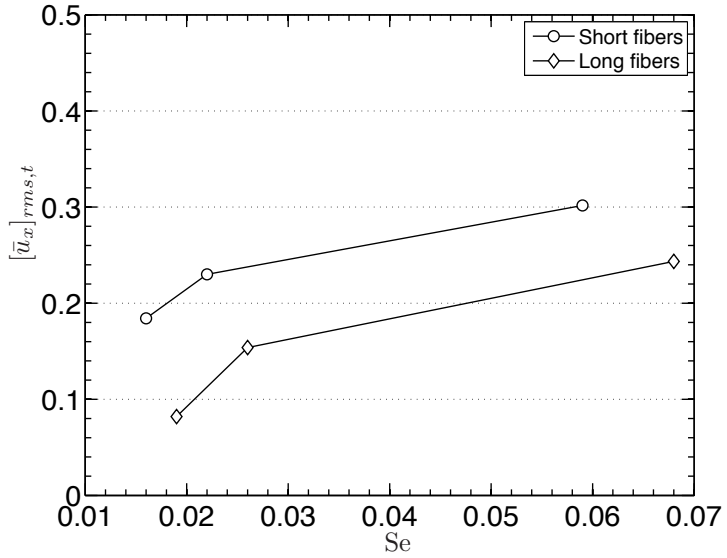

FIGURE 5.17. Average time fluctuations of $\bar{u}_x$ at y=-39 for long and short fibers, as a function of Se. ○: **Case A**, **Case C**, **Case E**. ◇: **Case B**, **Case D**, **Case F**. Each ○ and ◇ is calculated from the average of three realizations.

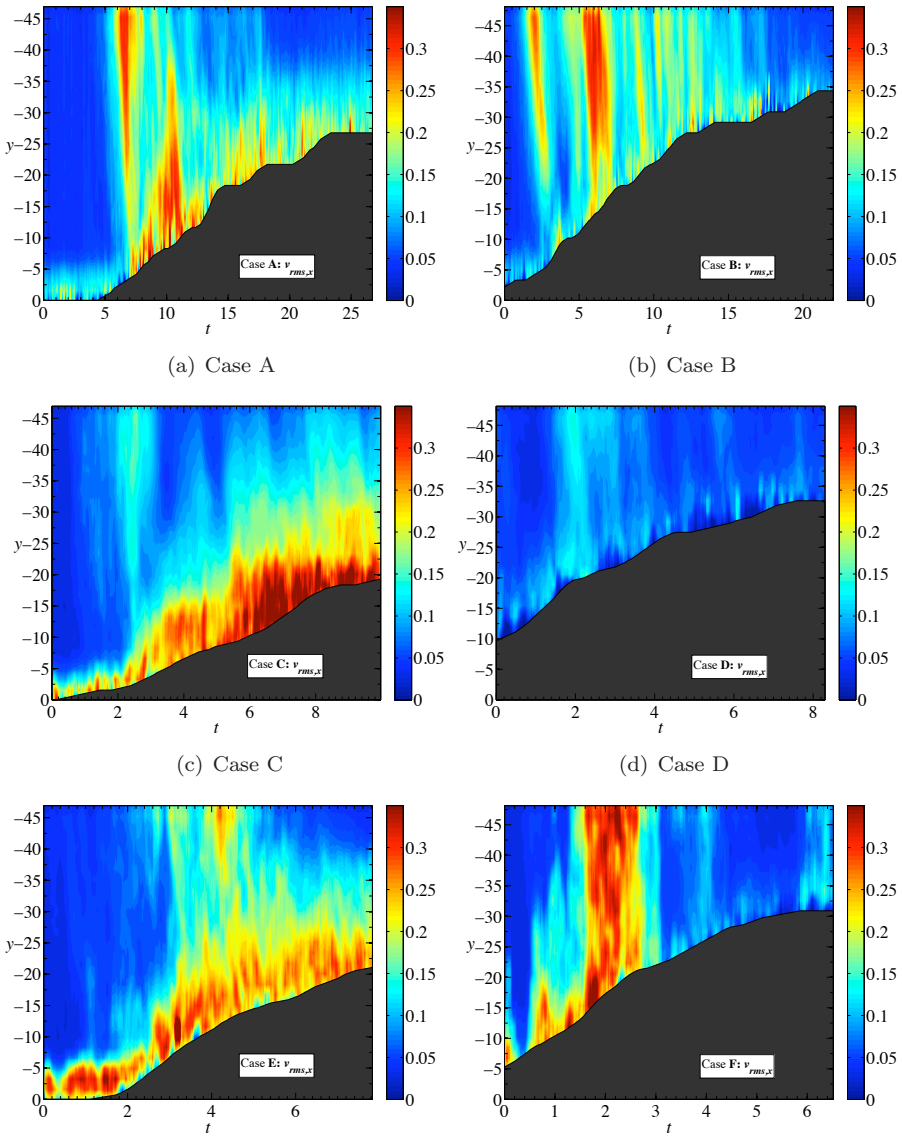

(a) Case A (b) Case B

(c) Case C (d) Case D

(e) Case E (f) Case F

FIGURE 5.18. Contours of $v_{rms,x}$ as a function t/t_s and y/d_f for all cases. The values are normalized with the corresponding V_m. The dark area at the bottom right of each figure shows the evolution of the average height of the fiber network, h_f. In this figure, $v_{rms,x}$ is obtained from the average of 3 realizations.

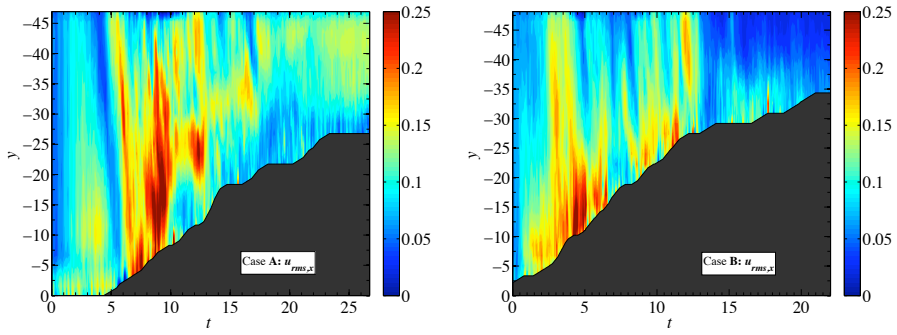

(a) Case A (b) Case B

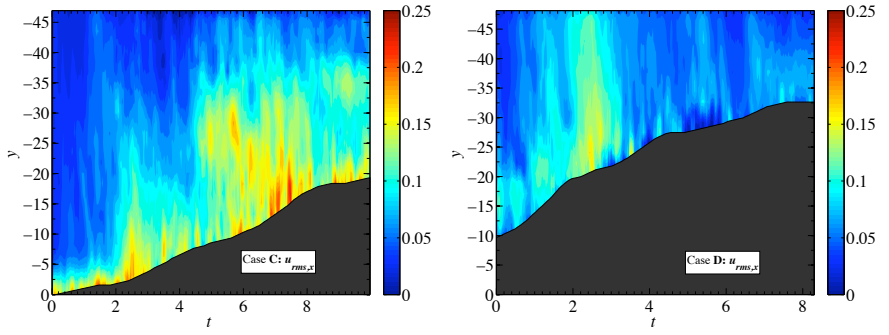

(c) Case C (d) Case D

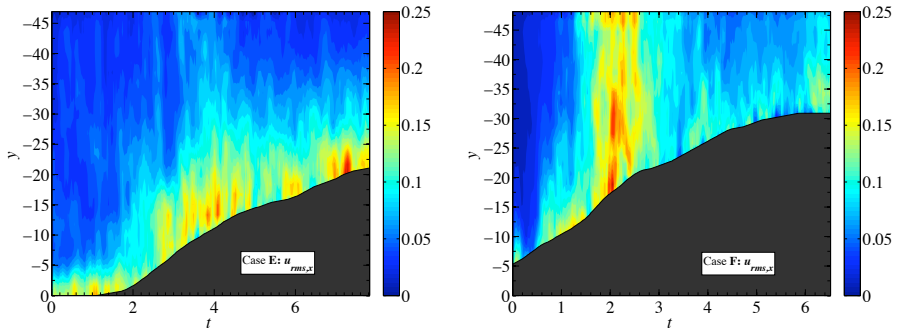

(e) Case E (f) Case F

FIGURE 5.19. Contours of $u_{rms,x}$ as a function t and y for all cases. The values are normalized with the corresponding V_m. The dark area at the bottom right of each figure shows the evolution of the average height of the fiber network, h_f. In this figure, $u_{rms,x}$ is obtained from the average of 3 realizations.

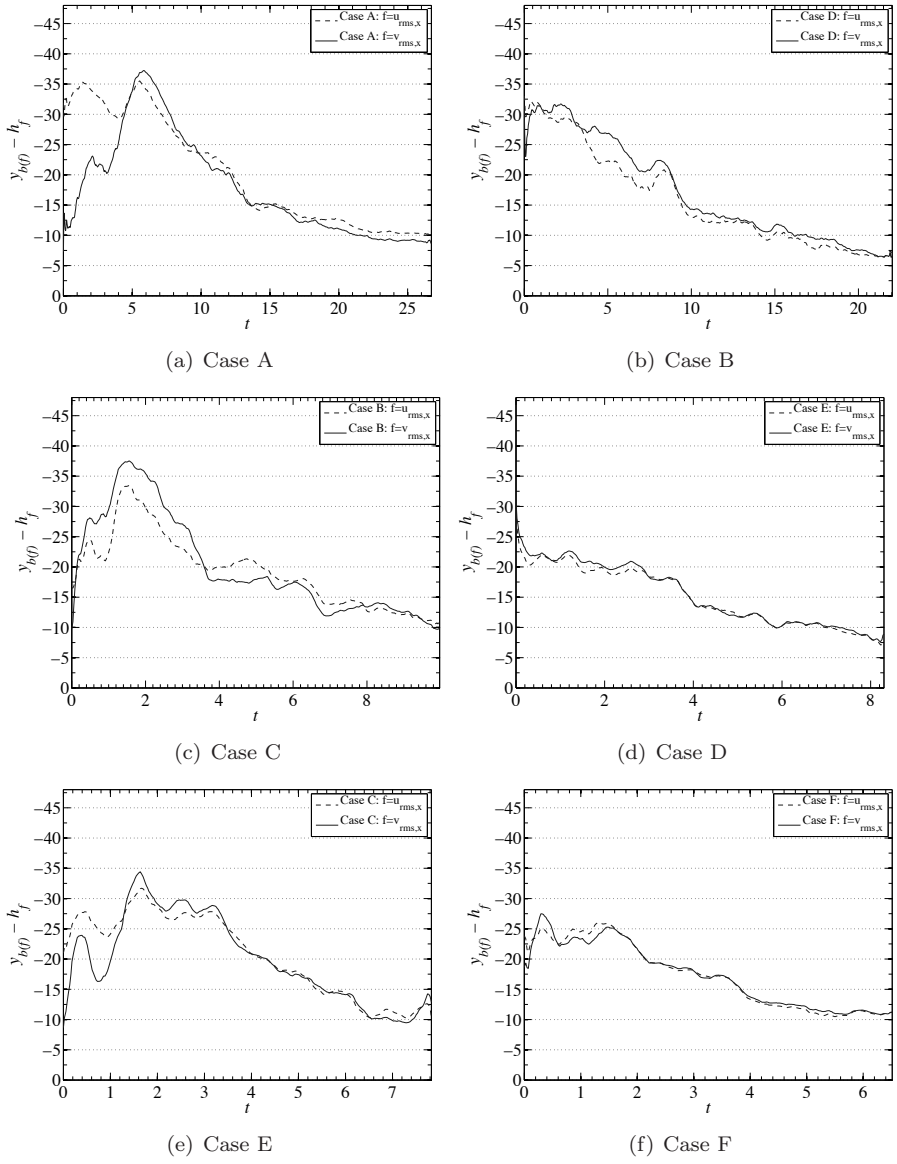

(a) Case A (b) Case B

(c) Case C (d) Case D

(e) Case E (f) Case F

FIGURE 5.20. The plots show the distance from the surface of the network at which the 85% of E_f is confined for all cases. The solid line (-) shows the case where $f = v_{rms,x}$, instead (- -) corresponds to $f = u_{rms,x}$. Each line is obtained from the average of 3 realizations.

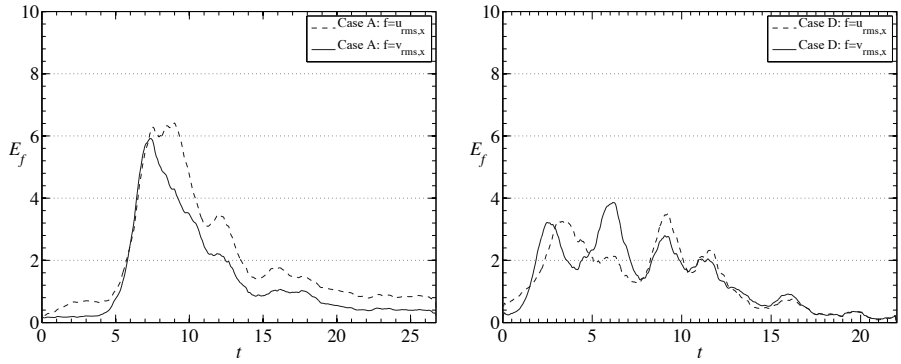

(a) Case A

(b) Case B

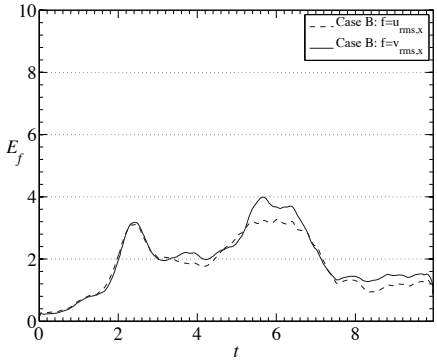

(c) Case C

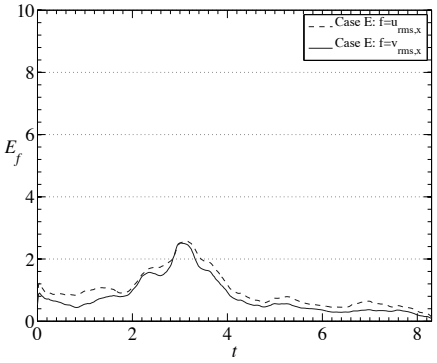

(d) Case D

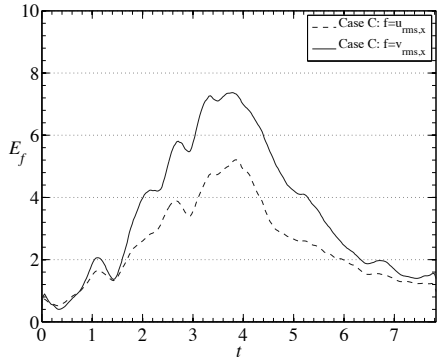

(e) Case E

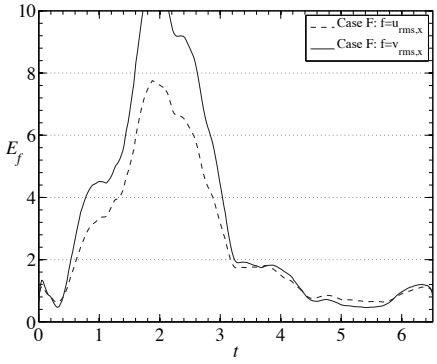

(f) Case F

FIGURE 5.21. Time evolution of E_f for all experimental cases. The solid line (-) shows the case where $f = v_{rms,x}$, instead (- -) corresponds to $f = u_{rms,x}$. Each line is obtained from the average of 3 realizations.

CHAPTER 6

Discussion

In the previous chapter we presented measurements of the mean and instantaneous velocity fields, above the empty screen and during the formation of the fiber network.

For the case with the empty screen, the flow was found to be stationary, but when fibers have been included in the suspension, the flow during the filtration became time dependent.

As discussed in chapter 2, the time dependancy is introduced by the forming fiber network on top of the screen (time dependent boundaries), by the inherent instability of the free sedimentation of the fibers, and by the coupling between the two phenomena.

Velocity fluctuations are important because they are connected to the transport of material inside the domain (large scales), or to the change of orientation distribution (small scales). Although the scales of the fluctuations have not been measured directly, we can still deduce them from the data in chapter 5.

In particular, the data contain measurements of small and large scale fluctuations.[1], where small scales are those that are of the order of the image window size, and large scales are fluctuations that take place on a scale larger than the image window.

6.1. Large scale fluctuations

In a closed domain with impervious walls, the average along horizontal lines of the vertical and horizontal velocity should be constant in time, if the flow rate is kept constant. In particular, the condition $\bar{v}_x$=V_m and $\bar{u}_x$=0 should be valid at every t.

Here however, the measurement domain is not confined within solid walls (the image window is only a portion of the total channel width), and a net inflow is allowed. Therefore, any deviation of $\bar{v}_x$ and $\bar{u}_x$ from V_m and 0, respectively,

[1] Typically, in fluid mechanics the term "fluctuations" is used to define the velocity variation in time around a mean value. In this case, we use it also to indicate a instantaneous variation in space.

must come from fluctuations that take place in the flow on a scale larger than the size of the measurement domain.

Figure 5.3 shows that when there are no fibers in the suspension, in a region far enough from the walls, there are no substantial large scale fluctuations.

Instead, when fibers are present, we have seen that $\bar{v}_x(t)$ and $\bar{u}_x(t)$ can diverge considerably from their respective average values (see figures 5.15 (a,b) and 5.16 (a,b)).

This can be due either to the effects of the sedimentation (*e.g.* large scales fluctuations generated by fiber flocs, Metzger *et al.* (2005)), or by perturbations introduced by the forming network.

However, the fact that the mean level of fluctuations is increasing with increasing Se (see figure 5.17), which measure the relative importance of the sedimentation, makes the former explanation more probable.

6.2. Small scale fluctuations and boundary region

Although large scales fluctuations can contribute to its value, the rms of the velocity profiles along horizontal lines is mainly a measure of fluctuations of the size of the image window and smaller.

Small scales are associated to regions with high strain rate and vorticity, which define the dynamics of the orientation distribution through equation 2.22.

6.2.1. *Effect of the screen*

At $t = 0$, when no fibers have entered the domain, small scales fluctuations are confined in a thin region close to the screen (see figures 5.6 and 5.7), whereas the rest of the domain is undisturbed. This is not surprising, since the only inhomogeneity in the flow is introduced by the sequence of wires and gaps from the screen.

On the base of these measurements, the height y_b of this boundary region has been defined in section 5.3.4. The extension of this region is $-5 < y_b/d_s < -1$ for all cases, and it is independent of Re_{d_s}, in the investigated range ($5 < \mathrm{Re}_{d_s} < 88$).

Moreover, figures 5.9 and 5.10 confirm that regions of high horizontal rms are correlated with regions of high strain and vorticity, and that the boundary region y_b is similar for all quantities.

6.2.2. *Effect of the forming network*

When fibers are present, the situation is more complex, since (i) there is a time dependent network structure on top of the screen and (ii) fluctuations are introduced by the fibers in the suspension.

Nevertheless, for the cases with long fibers (see figures 5.18 (a,c,e) and 5.19 (a,c,e)), a region of high amplitude activity of the small scales appears to

be confined close to the forming fiber network, although the extension of this region varies with the time.

Instead, looking at figures 5.18 (b,d,f) and 5.19 (b,d,f).This region is not as evident above a network formed with short fibers. This could be explained by the fact that short fibers form a network which has a different structure and average gap size (presumable more homogenous structure and smaller gaps).

The analysis of the boundary region y_b shows that this value is time dependent, and that this can be subjected to large variations in time (see figure 5.20). In general, we can observe an increase, followed by a decrease of the value of y_b. For long fibers (**Case A**, **Case C** and **Case E**) this length is about $10d_p$, whereas for short fibers (**Case B**, **Case D** and **Case F**) it is slightly lower. A similar behavior is observed for the total fluctuation energy E_f, shown in figure 5.21.

The conclusion is that the region where the small scale activity due to the boundary is directly coupled to the average gap size of (i) the screen at early times and (ii) of the forming network once at later times. Furthermore, the latter is varying in time, being more inhomogeneous in the beginning. In other words, the hypothesis $y_b/d = constant$, where d is the average gap size, found for (i), might also hold after the filtration has started ($t > 0$), so that the variation of y_b would be connected to d. To verify this hypothesis, measurements over steady networks of varying thickness could be made.

6.2.3. *Evaluation of the scaling parameters*

On the base of these measurements, one can estimate and discuss the values of the scaling parameters defined in section 2.6.

From the measured boundary region y_b and strain rate ϵ, we can calculate the parameter $T_r = y_b/(V_m T)$, where T is the period for a fiber to perform one Jeffery's orbit (see equation 2.19). T_r relates the residence time of a particle in the boundary region to the time required to perform a complete Jeffery's orbit. Thus it is a measure of how much the orientation distribution can change in the boundary region. The calculations show that $T_r < 0.05$ for all the cases, if y_b is taken from the measurements above the empty mesh. Therefore no significant variation of the orientation distribution can take place in this phase. This is also in agreement with qualitative visual inspections of the flow images. For the cases with fibers instead, the estimation of T_r is not possible since the instantaneous velocity gradients are not available. However, it is reasonable to assume that due to the increase of y_b, also T_r increases slightly.

It has to be pointed out that T_r does not say anything about the change in mass distribution, which can still occur in this region. In fact, more fibers should be transported towards the areas of higher mass flow (corresponding to the location of the gaps). However, calculating the change of mass distributions in the boundary region is not straightforward, since this phenomena depends

on the ratio between fiber length and gap size, as well as on fiber orientation, and it would require a detailed analysis based on the complete set of equations of motion.

The parameter H_s, which compares the importance of the sedimentation to that of the boundary region (see equation 2.30) can also be estimated from the measurements. First of all, one can observe that $H/y_b \ll 1$ and $V_m/V_s \ll 1$. Moreover, it was concluded that the extent of the boundary region was not dependent on the Reynolds number and that it scaled with the gap size. Hence one can write $y_b = Kd_p$, where K is a constant dependent on the network structure. With these observations the expression in (2.30) can be simplified as:

$$H_s \approx \frac{H - V_m t_s}{K d_p} \tag{6.1}$$

As expected, the effects of sedimentation become less and less important as V_m is increased (in agreement to what observed in section 6.1), and they are negligible when $V_m t_s > H$.

6.3. Future work

To understand the complex interactions between the forming network and the incoming flow, more measurements on a larger domain are needed, so that all the relevant scales can be properly measured and identified. Measurements of the flow structures require higher accuracy in the flow velocity measurements, which could be achieved with the use of a high power pulsed laser, a high resolution camera and fluorescent particles. These measurements could also be done over steady networks of different thickness, in order to investigate the effect of the different network structures.

However, in order to fully understand the complicated process of network forming the right approach is probably to combine experiments and calculations. Given the measured flow field fiber mass and orientation distribution can be estimated. For instance, this can be done using the slender body theory. Ultimately, such calculations should be verified against simultaneous measurements of the fluid and the fiber motion.

6.4. Relevance for papermaking

Although this is a laboratory experiment where factors like jet-wire speed difference, fillers *etc.*, are neglected, some of the observations are relevant for the industrial process of paper formations.

Table 2.1 shows that, even if the physical scales of the experiment are ten times larger than those of the papermaking process, the governing parameters typical of papermaking are in the same range as those of the experiments.

First of all, it appears from section 6.1 that to reduce large scale fluctuations (*i.e.* larger than a fiber length), which might lead to bad formation, it is important that the dewatering is done at speeds much higher than the sedimentation velocity of the fibers (as is the case in industrial papermaking).

Instead, from the analysis of the flow above the mesh, which is important to determine the orientation of the first fiber layer, we observed that the dewatering velocity is less relevant since the position of the boundary region does not depend on the Reynolds number and is proportional to the gap size. Moreover, we have seen that in that region T_r is too small for relevant change in fiber orientation to occur. The network structure is thus defined by the incoming suspension and the direct contact between the wire and the fibers.

However, when the network has begun to form, and the first fiber flocs has deposited on the screen, the size of the boundary region increases and scales with the floc size (thus approximately with the fiber length), hence, changes in fiber orientation due to the flow might be relevant.

The boundary region is also the region of non uniform dewatering velocity, which is responsible for the self-healing effect (Norman 1995). A complete description of the self healing effect is believed to be a complicated function dependent on fiber orientation, fiber aspect ratio and network structure.

Finally, the apparatus and the techniques developed in this work can be used for several applied studies. The most obvious is filler motion and accumulation during forming. The physics of this process is unknown to a large extent also on an empirical level. Insights would have a direct impact on the control and design of the product properties.

CHAPTER 7

Summary

This work is an experimental study of the flow generated during the filtration of a suspension of fibers through a semi-permeable screen.

The aim was to study the interaction between suspending fluid, fibers, screen and forming fiber network, and learn which parameters have a major impact on the dynamics of the formation of the fiber network.

The case under study is related to the industrial application of paper-making, where the filtration of a fiber suspension through a permeable screen represents the core of the entire process. Proper comparison with the industrial process was secured by analyzing the governing equations and derive the scaling parameters. This analysis was also necessary in order to understand how the measured quantities affect the network formation.

The first part of the work was to design and build an experimental apparatus where the filtration process could be realized and controlled. The setup includes a test section, a driving unit, together with custom made fibers and fluid with matched index of refraction. The filtration velocity can be accurately controlled and both fluid and fibers in a plane inside the test section can be visualized.

An in-house measurement system based on PIV and Image processing aimed at measuring the velocity field during the filtration process was also developed and validated. Three experiments are reported. The first two, without any fibers, are aimed at characterizing the flow in the test section in the near-wall region (i), and in the proximity of the screen (ii). For (i), the time evolution of the velocity profiles is investigated. A region not affected by the boundary layer was found for all the investigated cases. In that region, the flow was found to be stationary.

In (ii), experiments at three Reynolds number were conducted and it was concluded that the perturbations introduced by the screen are confined in a thin region (*boundary region*) close to the screen. The extension of the boundary region is independent of the Reynolds number based on the wire diameter of the screen.

In the third type of experiments fibers were introduced in the flow. We performed six experimental cases with different combinations of filtration velocity and fiber aspect ratio. The results showed that the flow becomes time dependent and large and small scales fluctuations can occur. The intensity of the large scale fluctuations were found to increase with a parameter that relates the sedimentation velocity of a single fiber to the average filtration velocity, thus we expect large scale fluctuations to be related to the effect of fiber sedimentation.

The small scales were found to be mostly confined near the fiber network, but occasionally, the region of small scales activity were diffused over the entire domain.

However, a boundary region could still be defined, but its extension from the network surface was found to be time dependent. The general trend that was observed was an increase followed by a decrease.

Based on these findings, we formulated the hypothesis that the extension of the boundary region is dependent on the average gap size of the fiber network.

Finally, the value of two scaling parameters T_r and H_S was estimated and used to quantify the (i) importance of sedimentation effects, and the (ii) possibility for the fibers to rotate under hydrodynamic interactions with the boundaries due to the filtration flow. The measurements together with the analysis show that these effects should be small in the industrial application.

Acknowledgements

This work has been financially supported by the *Biofibre Material Centre* (BiMaC), and by the *Swedish Energy Agency* (STEM) and it has been carried out within the research environment of the *Linné FLOW Centre*.

Many thanks go to my main supervisor Dr. Fredrik Lundell for patiently guiding me in the development of this project and for sharing with me his knowledge and endless curiosity. I would also like to thank my co-supervisor Dr. Daniel Söderberg for providing me with valuable research directions and for being the interpreter between my research and the world of papermaking.

My gratitude goes to Prof. Henrik Alfredsson, who first accepted me in the Fluid Physics laboratory at the department of Mechanics of KTH and to Prof. Alessandro Talamelli for transmitting to me his passion for fluid mechanics as well as for being a fun and sincere teacher and friend.

Thanks to our former toolmakers, Ulf Landén and Marcus Gällstedt, for manufacturing with skill the experimental apparatus and for the afternoon "fika" in the workshop, and to our current toolmakers Joakim Karlström and Göran Rådberg for always greeting me with a sincere happy mood, even when I ask them to solve my problems.

For the valuable and the "non-valuable" discussions, for the support and for bringing happiness to my days at the lab (and outside); for this and other, thanks to the friends I met at KTH mechanics: Veronica, Ramis, Thomas, Allan, Bengt, Charlotte, Outi, Timmy, Shiho, Enrico, Luca, Davide and all the others.

Outside the lab, first of all my gratitude goes to my family. Thanks for your love, encouragement and support. In all I do, you are my reference points.

Special thanks go to Federico and Lallo Giuliani, who taught me many things, including that "*la meccanica non è la moglie del meccanico*". Thanks to all my "italian" friends, starting from my flat mate Pablo and all you guys, that make me feel like home whenever and wherever we meet.

However, it would be impossible for me to reach this and any other goal without having a special person by my side. Grazie Sama.

References

Adanur, S. 1994 Effects of forming fabric structural parameters on sheet properties. *Tappi journal* **77**, 187–195.

Adrian, J. 1986 Image shifting technique to resolve directional ambiguity in double-pulsed velocimetry. *Applied Optics* **25**, 3855–3858.

Adrian, R. 2005 Twenty years of particle image velocimetry. *Experiments in Fluids* **39**, 159–169.

Barker, D. & Fourney, M. 1977 Measuring fluid velocities with speckle patterns. *Optics Letters* **1**, 135–137.

Batchelor, G. K. 1970 The stress system in a suspension of force-free particles. *J. Fluid Mech.* **41**, 545–570.

Becker, L. & Shelley, M. 2001 Instability of elastic filaments in shear flow yields first-normal-stress differences. *Phys. Rev. Lett.* **87** (19), 1–4.

Brenner, H. 1974 Rheology of a dilute suspension of axisymmetric brownian particles. *International Journal of Multiphase Flow* pp. 195–341.

Brown, M., Parsheh, M. & Aidun, C. 2006 Turbulent flow in a converging channel: effect of contraction and return to isotropy. *J. Fluid Mech.* **560**, 437–448.

Bürger, R., Concha, F. & Karlsen, K. H. 2001 Phenomenological model of filtration processes: 1. cake formation and expression. *Chemical Engineering Science* **56**, 4537–4553.

Butler, J. E. & Shaqfeh, E. S. G. 2002 Dynamic simulations of the inhomogeneous sedimentation of rigid fibres. *J. Fluid Mech.* **468**, 205–237.

Carlsson, A., Lundell, F. & Söderberg, L. 2007 Fiber orientation control related to papermaking. *Journal of Fluids Engineering* **129** (4), 457–468.

Chung, K., Simmons, M. & Barigou, M. 2007 A new piv approach to measuring gas and liquid phase velocities in a miniature stirred vessel. In *proceedings of 6th International Conference on Multiphase Flows, ICMF2007, July 9-13 2007*.

Clift, R., Grace, J. & Weber, M. 1978 *Bubbles, drops, and particles*. Academic Press.

Concha, F. & Bürger, R. 2002 A century of research in sedimentation and thickening. *KONA Powder and Particle* **20**, 38–48.

Cox, R. 1970 The motion of long slender bodies in a viscous fluid part 1. general theory. *Journal of Fluid Mechanics* **44**, 791–810.

Delnoij, E., Westerweel, J., Deen, N. & Kuipers, J. 1999 Ensemble correlation piv applied to bubble plumes rising in a bubble column. *Chemical Engineering Science* **54**, 5159–5171.

Deng, M. & Dodson, C. T. J. 1994 *Paper: An Engineered Stochastic Structure*. Tappi Press.

Doi, M. & Edwards, S. 1978 Dynamics of rod-like macromolecules in concentrated solution. part 2. *Journal of the Chemical Society* **74**.

Duda, R. & Hart, P. 1972 Use of the Hough transformation to detect lines and curves in pictures. *communications of the ACM* **15** (1), 11–15.

Dudderar, T. & Simpkins, P. 1977 Laser speckle photography in a fluid medium. *Nature* **270**, 45–47.

Enwald, H., Peirano, E. & Almstedt, A. 1996 Eulerian two-phase flow theory applied to fluidization. *International Journal of Multiphase Flow* **22**, 21–26.

Etuke, E. & Bonnecaze, R. 1998 Measurement of angular velocities using electrical impedance tomography. *Flow Measurement and Instrumentation* **9**, 159–169.

Grousson, R. & Mallick, S. 1977 Study of flow pattern in a fluid by scattered laser light. *Applied Optics* **16** (9), 2334–2336.

Guazzelli, É. 2001 Evolution of particle-velocity correlations in sedimentation. *Phys. Fluids* **13** (6).

Guazzelli, É. 2006 Sedimentation of small particles: how can such a simple problem be so difficult? *Comptes rendus-Mécanique* **334**, 539–544.

Hampson, P. 1998 Fibre length and fabric aperture. In *In proceeding of Appita 52th Annual Conference*, pp. 377–382.

Herzhaft, B. & Guazzelli, É. 1999 Experimental study of the sedimentation of dilute and semi-dilute suspensions of fibres. *J. Fluid Mech.* **384**, 133–158.

Herzig, R. & Johnson, D. 1999 Investigation of thin fiber mats formed at high velocity. *Tappi journal* **82** (1), 226–230.

Holm, R. 2005 Fluid mechanics of fibre suspensions related to papermaking. PhD thesis, KTH Mechanics, Stockholm, Sweden.

Holmqvist, C. 2005 Mechanical modelling of blade forming and drainage of flocculated suspensions. PhD thesis, KTH Mechanics, Stockholm, Sweden.

Honkanen, M. & Marjanen, K. 2007 Analysis of the overlapping images of irregularly-shaped particles, bubbles and droplets. In *proceedings of 6th International Conference on Multiphase Flows, ICMF2007, July 9-13 2007*, p. 13.

Hyensjö, M. & Dahlkild, A. 2008 Study of the rotational diffusivity coefficient of fibres in planar contracting flows with varying turbulence levels. *International Journal of Multiphase Flow* (In press).

Jacob, M. & Unser, M. 2004 Design of steerable filters for feature detection using canny-like criteria. *IEEE Transactions on pattern analysis and machine intelligence* **26** (8), 1007–1019.

Jeffery, G. 1922 The motion of ellipsoidal particles immersed in a viscous fluid. *Proceedings of the Royal Society of London.* pp. 161–179.

Jong, J., Baines, W. & Currie, I. 1999 Experimental characteristics of forming fabrics and fibre mats. *Journal of pulp and paper science* **25**, 95–99.

Kao, S. & Mason, S. 1975 Dispersion of particles by shear. *Nature* **253**, 619–621.

Keane, R. & Adrian, R. 1991 Optimization of particle image velocimeters. *Measurement Science and Technology* **2**, 963–974.

Keller, J. & Rubinow, S. 1975 Slender-body theory for slow viscous flow. *Journal of Fluid Mechanics* **75**, 705–714.

Koch, D. & Shaqfeh, E. 1989 The instability of a dispersion of sedimenting spheroids. *Journal of Fluid Mechanics Digital Archive* **209**, 521–542.

Lucisano, M. & Norman, B. 1994 The forming and properties of quasi-random laboratory paper sheets. In *proceedings from the 1994 International Paper Physics Conference, San Diego, California.*.

Mackaplow, M. & Shaqfeh, E. 1998 A numerical study of the sedimentation of fibre suspensions. *J. Fluid Mech.* **376**, 149–182.

Metzger, B., Butlerz, J. E. & Guazzelli, E. 2007 Experimental investigation of the instability of a sedimenting suspension of fibres. *J. Fluid Mech.* **575**, 307–332.

Metzger, B., Guazzelli, E. & Butler, J. 2005 Large-scale streamers in the sedimentation of a dilute fiber suspension. *Phys. Rev. Lett.* **95** (16), 1–4.

Norman, B. 1995 The effect of localised dewatering in paper formation. In *Proceedings of Internationnal paper physics conference, San Diego*.

Olson, J. & Kerekes, R. 1998 The motion of fibres in turbulent flow. *J. Fluid Mech.* **377**, 47–64.

Petrie, C. 1999 The rheology of fibre suspensions. *Journal of Non-Newtonian Fluid Mechanics* **87**, 369–402.

Pickering, C. & Halliwell, N. 1984 Laser speckle photography and particle image velocimetry photographic film noise. *Applied Optics* **23** (17), 2961–2969.

Powell, R. L. 2008 Experimental techniques for multiphase flows. *Physics of Fluids* **20** (040605), 1–21.

Quraishi, S. 1989 *A survey of the development of papermaking in Islamic Countries*, , vol. 3. Bookbinder.

Raffel, M. W. C. K. J. 1998 *Particle Image Velocimetry*. Springer.

Sampson, W., McAlpin, J., Kropholler, H. & Dodson, C. 1995 Hydrodynamic smoothing in the sheet forming process. *Journal of pulp and paper science* **21** (12), J422–426.

Scharcanski, J. & Dodson, C. 1996*a* Neural network model for paper forming process. *Pulp and Paper Industry Technical Conference* .

Scharcanski, J. & Dodson, C. 1996*b* Neural network model for paper forming process. *IEEE Transactions on industry applications* **33**, 826–839.

Seymour, J., Maneval, J., McCarthy, K. & McCarthy, M. 1993 Nmr velocity phase encoded measurements of fibrous suspensions. *Physics of Fluids A: Fluid Dynamics* **5** (11), 3010–3012.

Shin, M. & Koch, D. 2005 Rotational and translational dispersion of fibres in isotropic turbulent flows. *J. Fluid Mech.* **540**, 143–173.

Söderberg, D. 1999 Hydrodynamics of plane liquid jets aimed at applications inpaper manufacturing. PhD thesis, KTH Mechanics, Stockholm, Sweden.

Stanislas, M., Okamoto, K., Kähler, C. & Westerweel, J. 2005 Main results of the second international piv challenge. *Experiments in Fluids* **39**, 170–191.

Stockman, G. & Agrawala, A. 1977 Equivalence of hough curve detection to template matching. *Communications of the ACM* **20** (11), 820–822.

Stover, C., Koch, D. & Cohen, C. 1992 Observations of fibre orientation in simple shear flow of semi-dilute suspensions. *Journal of Fluid Mechanics Digital Archive* **238**, 277–296.

Tornberg, A. 2004 Simulating the dynamics and interactions of flexible fibers in stokes flows. *Journal of Computational Physics* **196** (1), 8–40.

Tornberg, A. & Gustavsson, K. 2006 A numerical method for simulations of rigid fiber suspensions. *Journal of Computational Physics* **215** (1), 172–196.

Towers, D., Towers, C., Buckberry, C. & Reeves, M. 1999 A colour piv system employing fluorescent particles for two-phase flow measurements. *Measurement Science and Technology* **10**, 824–830.

Turney, M., Cheung, M., Powell, R. & McCarthy, M. 1995 Hindered settling of rod-like particles measured with magnetic resonance imaging. *AIChE Journal* **41** (2), 251–257.

Vomhoff, H. 1998 Dynamic compressibility of water-saturated fibre networks and influence of local stress variations. PhD thesis, KTH Mechanics, Stockholm, Sweden.

Wang, T., Wang, J., Ren, F. & Jin, Y. 2003 Application of doppler ultrasound velocimetry in multiphase flow. *Chemical Engineering Journal* **92**, 111–122.

Westerweel, J. 1997 Fundamentals of digital particle image velocimetry. *Measurement Science and Technology* **8**, 1379–1392.

Young, E., Martinez, D., Olson, J. & Buckley, K. 2006 The sedimentation of papermaking fibers. *AIChE Journal* **52** (8), 2697–2706.

Zirnsak, M., Hur, D. & Boger, D. 1994 Normal stresses in fibre suspensions. *Journal of Non-Newtonian Fluid Mechanics* **54**, 153–193.